Ocean Dynamics (2015) 65:1643–1663
DOI 10.1007/s10236-015-0891-1

Coastal ocean variability in the US Pacific Northwest region: seasonal patterns, winter circulation, and the influence of the 2009–2010 El Niño

Scott M. Durski[1] · Alexander L. Kurapov[1] · John S. Allen[1] · P. Michael Kosro[1] · Gary D. Egbert[1] · R. Kipp Shearman[1] · John A. Barth[1]

Received: 6 February 2015 / Accepted: 24 September 2015 / Published online: 26 October 2015

Abstract A 2-km horizontal resolution ocean circulation model is developed for a large coastal region along the US Pacific Northwest (34–50N) to study how continental shelf, slope, and interior ocean variability influence each other. The model has been run for the time period September 2008–May 2011, driven by realistic surface momentum and heat fluxes obtained from an atmospheric model and lateral boundary conditions obtained from nesting in a global ocean model. The solution compares favorably to satellite measurements of sea surface temperature and sea surface height, observations of surface currents by high-frequency radars, mooring temperature time series, and glider temperature and salinity sections. The analysis is focused on the seasonal response of the coastal ocean with particular emphasis on the winter circulation patterns which have previously garnered relatively little attention. Interannual variability is examined through a comparison of the 2009–2010 winter influenced by El Niño and the winters in the preceding and following years. Strong northward winds combined with reduced surface cooling along the coast north of Cape Mendocino (40.4N) in winter 2009–2010, resulting in a vigorous downwelling season, characterized by relatively energetic northward currents and warmer ocean temperatures over the continental shelf and upper slope. An analysis of the time variability of the volume-averaged temperature and salinity in a coastal control volume (CV), that extends from 41 to 47N and offshore from the coast to the 200-m isobath, clearly shows relevant integrated characteristics of the annual cycle and the transitions between winter shelf circulation forced by northward winds and the summer circulation driven primarily by southward, upwelling-favorable winds. The analysis also reveals interesting interannual differences in these characteristics. In particular, the CV volume-average temperature remains notably warmer during January–March 2010 of the El Niño winter.

Keywords Coastal ocean variability · El Nino · Coastal ocean modeling · Northeast Pacific · Downwelling

Responsible Editor: Emil Vassilev Stanev

This article is part of the Topical Collection on *Coastal Ocean Forecasting Science supported by the GODAE OceanView Coastal Oceans and Shelf Seas Task Team (COSS-TT)*

✉ Scott M. Durski
sdurski@coas.oregonstate.edu

[1] College of Earth, Ocean and Atmospheric Sciences, Oregon State University, Corvallis, OR, USA

1 Introduction

The region along the US West Coast between Juan de Fuca Strait (48.5N) and Point Conception (34.4N) is known to be an area of intense wind-driven upwelling in summer. North of Cape Mendocino, after upwelling conditions relax during the autumn, predominantly northward winds drive downwelling and northward alongshore currents in winter. The upwelling dynamics and their influence on the physical, chemical, and biological characteristics of the coastal ocean have been the focus of many studies using in situ and satellite observations, idealized numerical models, and realistic computer simulations (e.g., Barth and Wheeler, 2005 and other papers in that special issue summarizing results from the Coastal Ocean Advances in Shelf Transport (COAST) program). The winter downwelling regime is relatively less sampled and studied than summer upwelling, in part because of logistical constraints collecting observations in winter storm conditions. Modeling studies of the downwelling regime have been limited to idealized situations. For example, Allen

and Newberger (1995) utilized a two-dimensional (cross-shore and vertical coordinates) model to discuss cross-shore and vertical transport associated with the development of a downwelling front. Whitney and Allen (2009a, b) analyzed dynamics of flows around banks in both upwelling and downwelling conditions using an alongshore periodic channel and spatially uniform winds. The possibility that interannual variability in winter downwelling may predetermine the intensity of coastal hypoxia in summer was recently studied using data analysis and idealized model simulations by Walters (2014). To the best of our knowledge, there has not been a study of US Pacific Northwest shelf circulation based on a realistic model simulation and focused on the winter downwelling regime.

Interannual variability in the coastal ocean circulation along the US west coast correlates with large-scale patterns, including the Pacific Decadal Oscillation (PDO) (Mantua et al. 1997, Chhak and Di Lorenzo, 2007) and El Niño (McPhaden, 1999; Huyer et al. 2002, Chavez et al. 2002, and other papers in that special issue, on the effect of the 1997–1998 El Niño). El Niño events are associated with a warm near-surface ocean temperature anomaly propagating along the equator toward the east and then continuing as baroclinic Kelvin waves along western coasts of North and South America. The El Niño signal propagating alongshore may influence coastal ocean environments of the Pacific Northwest by deepening the isopycnal surfaces along the continental slope. That change in the isopycnal slope would be dynamically balanced by a stronger poleward subsurface flow (undercurrent), changing temperature-salinity properties on a given isopycnal surface (see Huyer et al. 2002).

The atmospheric circulation pattern correlated with El Niño also impacts the region through an atmospheric teleconnection mechanism (Schwing et al. 2002). In response to anomalous ocean conditions in the equatorial region, atmospheric perturbations will propagate across the North Pacific and result in warmer conditions and cyclonic wind anomalies along the Pacific West Coast. The transition to El Niño conditions, e.g., as determined by the multivariate ENSO index (MEI; Wolter 1987), (Fig. 1), usually occurs in spring while the peak index values register in December–January. In response to El Niño, the ocean off the US West Coast begins to exhibit warmer conditions in summer. Anomalously warmer ocean temperatures and stronger northward winds are typically found during the following winter.

The study presented here was motivated by several needs. We have developed a high-resolution regional ocean model with the overarching goal to study influences between ocean interior and coastal ocean processes along the US West Coast. The model resolution is 2 km in the horizontal and the model domain spans north-south along the coast between 35 and 50N. The model simulation is performed for the 32-month period from October 2008 to May 2011. This paper presents analysis of the model performance over the full simulation. Particular emphasis is placed on the winter dynamics both to aid in the interpretation of the annual cycle and interannual variability and to supplement the rather limited literature describing the dynamics in this season. The strongest impetus for interannual variability during this study period is indeed the "moderate" 2009–2010 El Niño event and the subsequent strong La Niña phase in 2010–2011. To provide insight into interannual variability, we focus on the peak El Niño season, winter, and examine the three winters (2008–2009, 2009–2010, and 2010–2011) in detail. The model set-up is described in Section 2. In Section 3, we review the main features of ENSO over the study period and the potential impact on winter-forcing conditions for the domain of interest. In Section 4, we present model-data comparisons and discuss how the model represents coastal circulation features in winter and compare ocean response during the 2009–2010 El Niño winter to the preceding and following ones. In Section 5, time variability of the integrated heat and salinity balance for a specified control volume over the shelf off Oregon and southern Washington is discussed, with an emphasis on a contrast of the behavior during winter compared to that in summer and on the effects of the 2009–2010 El Niño. Section 6 provides the summary.

2 Model setup

Our model is based on the Regional Ocean Modeling System (ROMS, www.myroms.org), a free-surface, nonlinear, primitive equation model featuring terrain-following coordinates in the vertical and advanced numerics (Shchepetkin and McWilliams 2003, 2005). The Mellor-Yamada 2.5 scheme (Mellor and Yamada 1982) is utilized to parameterize vertical turbulence at subgrid scales. Dissipation of momentum along s-coordinates is treated as a harmonic viscosity with a coefficient of 5 $m^2\ s^{-1}$.

The domain extends from 34.5N (just north of Point Conception and the Santa Barbara channel) to 50N (the middle of Vancouver Island, British Columbia, Canada) and from 134W eastward to the coast. The alongshore extent of the model is chosen to capture the entire area of intensive seasonal upwelling and to possibly represent correctly the influences of the poleward slope current and coastally trapped waves on the dynamics off northern California, Oregon, and Washington. The model is discretized on a regular longitude-latitude grid. The resolution is approximately 2 km in the horizontal and 40 terrain-following layers in the vertical, with relatively better resolution near the surface and bottom.

Atmospheric forcing is obtained using a bulk flux formulation (Fairall et al. 1996). The required atmospheric fields (including the near-surface wind speed and direction, air

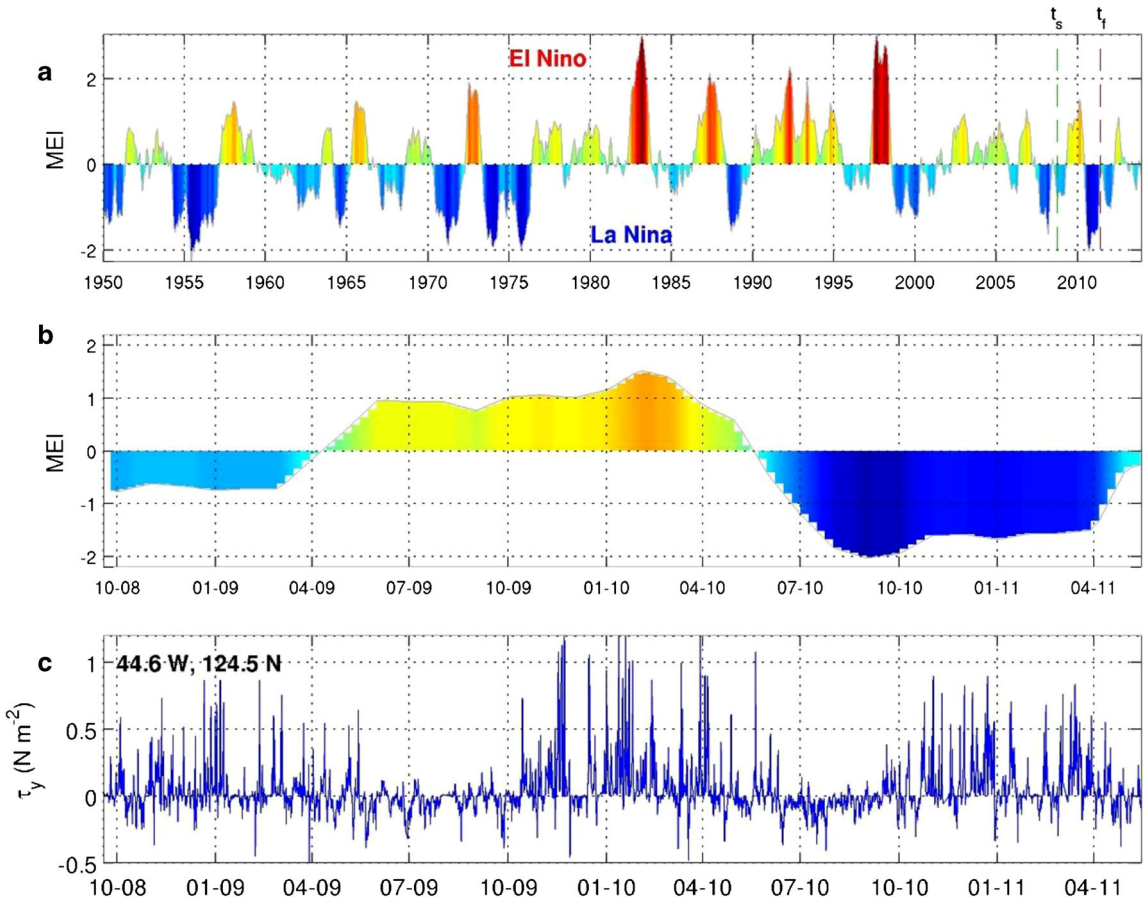

Fig. 1 **a** The multivariate ENSO index, MEI (Wolter, 1987), 1996–2014, **b** MEI for the duration of the model simulation, **c** the north-south wind stress time series over Oregon shelf (Heceta Bank complex, 44.65N, 124.5N). t_s and t_f in (**a**) indicate the start and finish of the model simulation

pressure, incoming shortwave, relative humidity, air temperature, and cloud cover) are obtained from the 12-km resolution National Oceanic and Atmospheric Administration North American Model (NOAA NAM). The atmospheric fields are provided every 6 h, resolving intense winter storms moving rapidly through the area.

Subtidal boundary conditions are obtained from the 1/12th degree resolution data assimilative global Hybrid Coordinate Ocean Model (HYCOM, www.hycom.org, Chassignet et al. 2005), implemented by the US Navy. The HYCOM outputs have been provided as instantaneous fields once a day. The inertial motions are aliased in such a record, showing up as strong oscillations in velocity fields, e.g., with an approximately 2.8-day period at 45N. This signal has been removed from the HYCOM-derived boundary conditions using a 5-day half-amplitude low-pass filter. We have confirmed that, at the south boundary of our domain within 100 km from the coast, HYCOM (which assimilates ARGO profiler temperature (T) and salinity (S) data) places the 26.5 kg m^{-3} isopycnal surface deeper in winter 2009–2010 than in the preceding and following winters, by about 20 m, consistent with the findings of Todd et al. (2011). To enforce this difference in ROMS, we had to "clamp" (in ROMS terminology) T and S at the south boundary to the HYCOM values. This resulted in an improvement in peak currents during January 2010 over the Oregon shelf, compared to our initial implementation, in which ROMS interior temperature and salinity near the boundary were nudged to the boundary values using the "radiation-plus-nudging" ROMS boundary conditions (Marchesiello et al. 2001). The latter boundary condition is still used on the western and northern boundaries with a nudging time scale on inflow of 3 days and 9 days on outflow. Tidal forcing, which might have some effect on cross-shelf exchange, is neglected in this model as it does not resolve the O (1 km) tidal excursion typical of the West Coast shelf (Kurapov et al. 2003, Osborne et al. 2011, 2014). No fresh water fluxes (precipitation-evaporation or rivers) are applied.

The model has been run for a 32-month period, starting from initial conditions provided by interpolation of HYCOM fields on October 1, 2008. Oceanic fields are saved as daily averages once every day. Note that no data assimilation of any kind, or nudging to climatology, was implemented in the model interior, facilitating analysis of dynamically balanced fields.

3 The 2009–2010 El Niño effects along the US Pacific Northwest coast

Although the 2009–2010 El Niño was much weaker than the major event of 1997–1998, it was the strongest since that time (Fig. 1). The multi-decadal MEI time series suggests that events of this strength are rather common. Based on synthesis of observations, Bjorkstedt et al. (2010) and Todd et al. (2011) concluded that the 2009–2010 El Niño influenced the US West Coast mainly through the atmospheric teleconnection mechanism. Ocean waters off the coasts of north California, Oregon, and Washington were anomalously warm, compared to long-term means, beginning June 2009. This anomaly persisted through the 2009–2010 winter and was interrupted in April 2010 by a series of strong upwelling events and transition to La Niña conditions on a basin scale. Let us note that while the 2009–2010 El Niño is qualified as "moderate" or "weak," the La Niña event beginning spring 2010 was the strongest in the last 25 years (see Fig. 1a). We have utilized a long time series from the NCEP atmospheric reanalysis product (http://www.esrl.noaa.gov/psd/data/gridded/data.ncep.reanalysis.html, Kalnay et al. 1996) to confirm that the downwelling-favorable wind anomaly was strongly positive during the El Niño winter, compared to the long-term mean (not shown here). Presumably, this led to intensified downwelling circulation. Todd et al. (2011) analyzed glider cross-shore hydrographic sections between 31 and 36N and found that the depth of the 26.0 kg m^{-3} isopycnal surface (used as a proxy of the position of the main thermocline) was lower in winter 2009–2010 than a 6-year average, but only by 20 m. Analysis of temperature and salinity on this isopycnal level did not reveal differences that would indicate anomalously strong poleward advection.

Comparisons of the atmospheric heat flux into the model, averaged in space over the entire domain and low-pass filtered (Fig. 2), suggest that the ocean received excessive warming that might be associated with the ENSO effect. Averaged over the El Niño period from June 2009 through March 2010 net heat flux into the ocean was 12 W m^{-2} larger than in the following La Niña period (June 2009 through March 2010). During the El Niño winter (December 2009 through March 2010), the heat flux was on average larger (less negative) by about 15 W m^{-2} compared to the preceding and following winters.

3.1 Winter wind forcing conditions

Although winters along the northwest US coast are in general characterized by downwelling-favorable northward winds, there is significant variability in the timing of the onset and termination of the downwelling season as well as in the persistence and strength of downwelling conditions over the course of the season. To describe the three winters presented here, we refer to the time series of the north-south wind stress at a shelf location at 44.65N, 124.5N (Heceta Bank complex, Oregon), shown in Fig. 1c, a map of winter-averaged wind stress over the domain (Fig. 3) and the time-latitude near-coastal north-south wind stress displayed in Fig. 4a. At

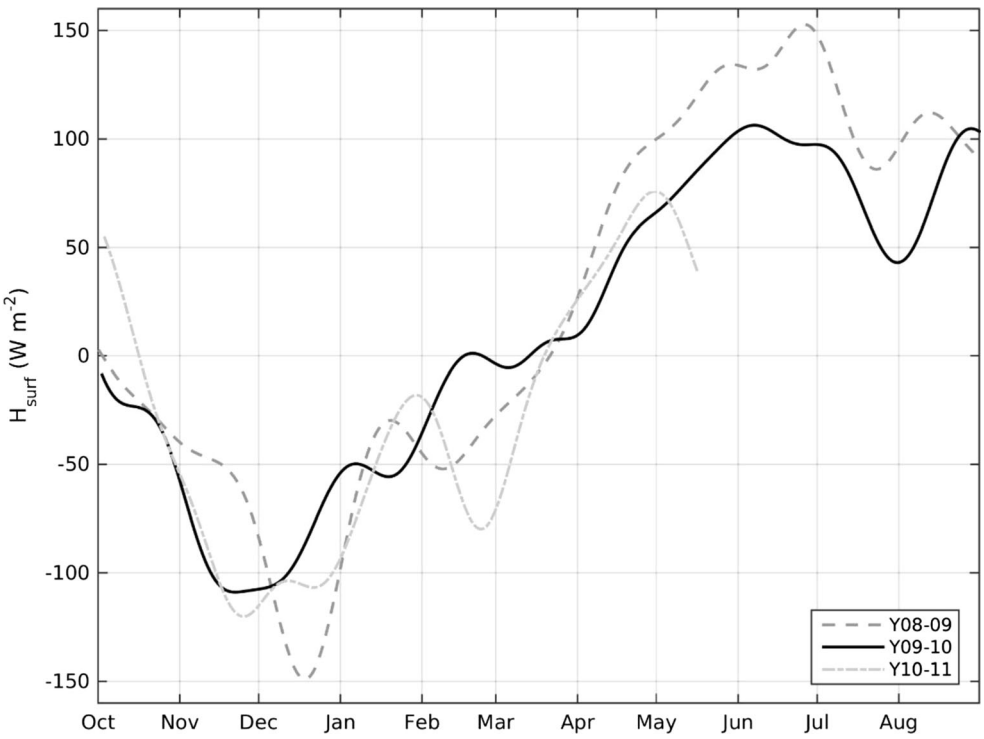

Fig. 2 Time series of monthly averaged low-pass filtered (60-day) and area-averaged (full model domain) atmospheric heat flux, October 2008–September 2009, October 2009–September 2010, and October 2010–May 2011

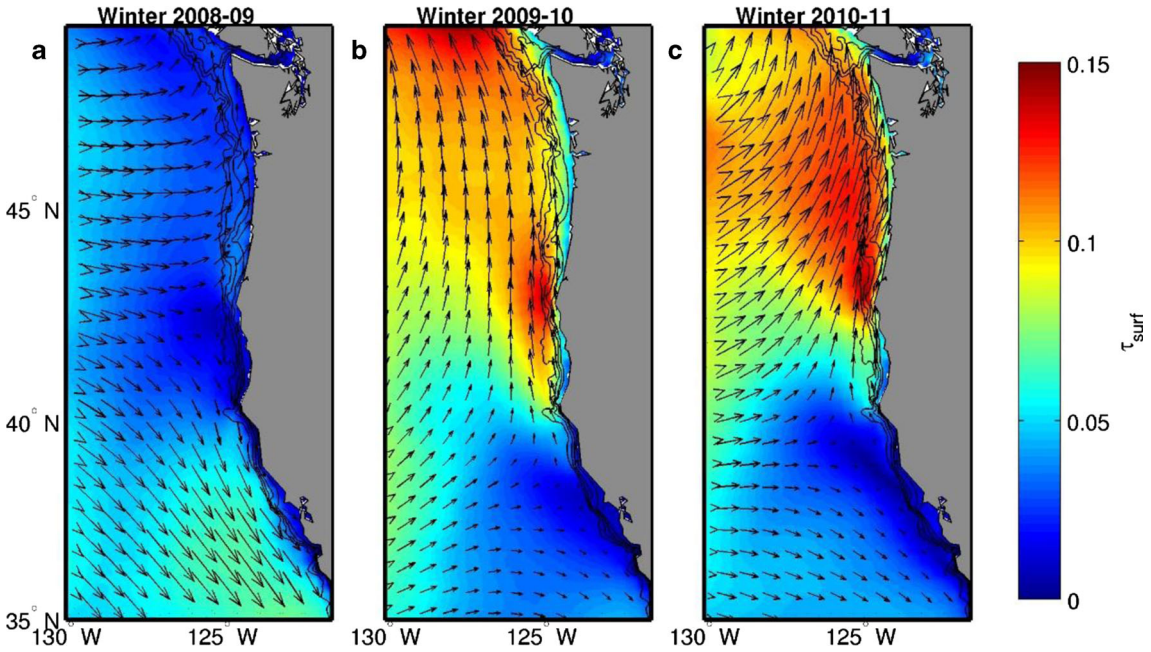

Fig. 3 The winter (DJFM)-averaged wind stress vectors and magnitude (*color*): **a** 2008–2009, **b** 2009–2010, **c** 2010–2011

44.65N, and along much of the Oregon-Washington shelf, the winds are much stronger in winter than in summer. Strong (>0.3 N m^{-2}), but short-lived (a few days), storms are a common occurrence. On average, winds in winter 2008–2009 are weaker than in the two following winters. While we believe that the strong winter winds along the coast in 2009–2010 are related to the large-scale atmospheric setup associated with ENSO, we note that the winds in 2010–2011 are frequently as strong as in 2009–2010, i.e., winters with wind events of this strength are not uniquely attributed to El Niño seasons.

The largest downwelling-favorable wind events happen during different parts of each winter, often with relaxations or even reversals in between. In winter 2008–2009, relatively strong northward wind events occurred at the turn of the year and in mid-February. In winter 2009–10, a strong storm took place in November 2009, followed by a weak reversal and then a return to energetic and near-persistent downwelling wind conditions through much of January and into February 2010. Winter 2010–2011 exhibited downwelling-favorable conditions through much of December, followed by only intermittent wind events in January and February and a return to prevailing downwelling-favorable winds through much of March 2011. In the following analyses, we pick a different month in each winter (February 2009, January 2010, and March 2011) to analyze ocean conditions during peak downwelling-favorable wind conditions.

Variability in the wind stress is generally coherent along the entire coast (Fig. 4), but winter winds are typically stronger in the north. Maps over the full domain of winter-averaged (December through March) wind stress magnitude and direction reinforce this point and reiterate that seasonally averaged winds were much weaker over the entire area in winter 2008–2009 than in the other 2 years. The north-south extent of the region of energetic near-coastal northward winds varies among the years, with strong winds extending considerably farther south in winters 2009–2010 and 2010–2011 than in 2009–2010. Accordingly, the location of the bifurcation point between the area of the downwelling- and upwelling-favorable winds along the coast differs. In 2008–2009, the separation is found near 43N, around Cape Blanco, with, in addition, comparatively strong upwelling-favorable conditions prevailing south of 40N. In contrast, in 2009–2010 and 2010–2011, the bifurcation point occurs at locations south of 40N with nearly negligible upwelling-favorable winds along the shelf to the south.

4 Model-data comparisons

In this section, we start by comparing the near-coastal, large alongshore scale, time and latitudinal behavior of model sea surface temperature (SST) and sea surface height (SSH) with corresponding satellite observations over the total 32-month time period. To do so, we also present the time-latitude behavior of the near-coastal alongshore wind stress and the resulting ocean model near-coastal alongshore surface currents. These figures are effective at showing the general characteristics of the winter coastal flow regimes and how they fit as part of the annual cycle at each latitude. They also illustrate some of the relevant near-coastal aspects of the interannual variability related to El Niño. We then go on to focus on the three winters within the study period, show additional model-data comparisons to establish confidence in the model accuracy, describe

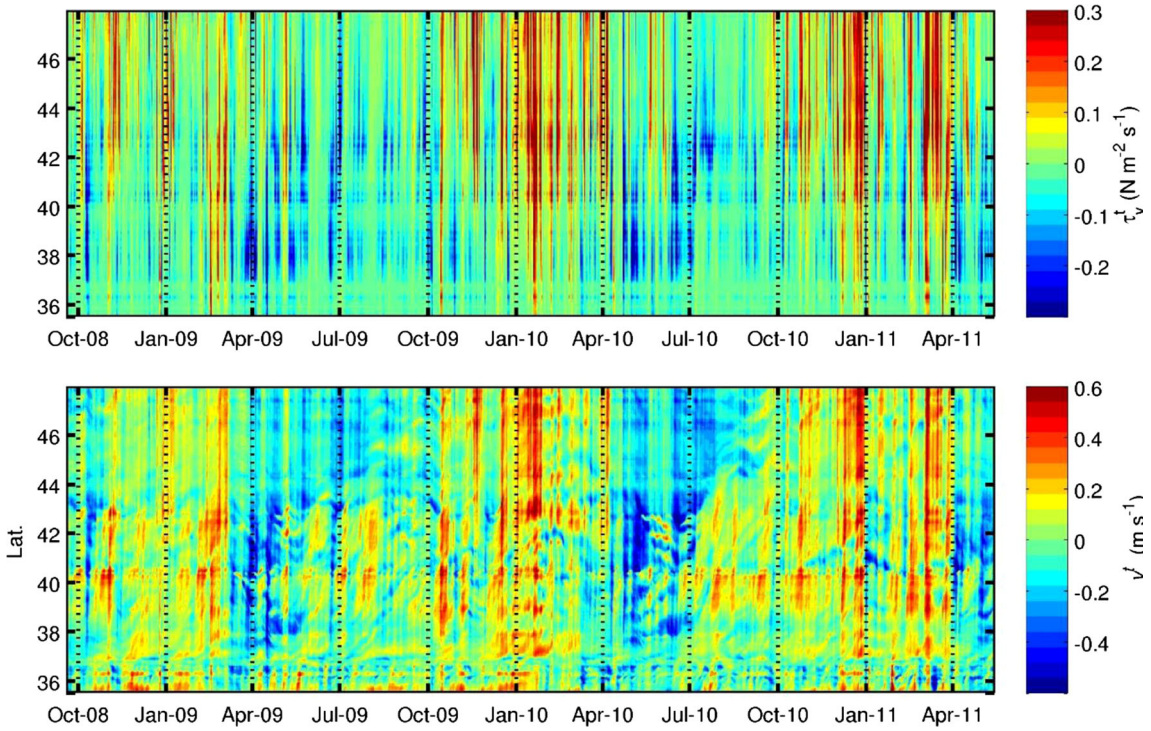

Fig. 4 (*Top*) Alongshore wind stress averaged between the coast and the 200-m isobath and (*bottom*) the model alongshore surface current averaged between the coast and the 200-m isobath

some of the basic circulation features associated with winter downwelling, and discuss some of the interannual differences in the model ocean response during winter.

4.1 Seasonal and interannual variability in the near-coastal region

The near-coastal alongshore wind stresses used for atmospheric forcing, averaged in the cross-shore direction between the coast and the 200-m isobath, and the ocean model alongshore surface currents, averaged across shore in a similar manner, are shown in Fig. 4. The general seasonal variability of the wind stress, dominantly northward in winter (October–March) and dominantly southward in summer (April–September) is evident. The latitudinal variation in magnitude of the northward winter wind stress, being typically stronger toward the northern part of the domain, is also clear as is the variation in magnitude of the summer southward wind stress, which is typically stronger in the south. The near-coastal alongshore surface currents show a seasonal variability that mostly corresponds to that expected from a response to the wind stress, i.e., northward in winter and southward in summer. The northward (southward) alongshore currents are typically accompanied by positive (negative) SSH fluctuations (Fig. 4) as anticipated from a geostrophic balance in the cross-shore direction. An interesting exception in the seasonal behavior of the alongshore currents occurs south of about 43N during late summer/fall (July–September) when the wind stress along the entire coast is still southward, but the surface currents have a considerable fraction of northward fluctuations. This type of behavior has been observed by Ramp and Bahr (2008) in current meter measurements from south of Cape Blanco at 42.44N on the shelf in 73 m water depth from May 2000 to October 2003. Ramp and Bahr (2008) associated this behavior with forcing by a poleward pressure gradient taking place during a dynamical season defined by ocean events and labeled as "autumn," which occurs between summer and winter. They noted that the start of the autumn season was variable and not clearly identifiable with specific events, but that the end, termed the "autumn transition," was clearly associated with the relatively abrupt cessation of southward upwelling-favorable winds and the start of northward winter winds, a behavior that is also visible in Fig. 4.

The model SSH averaged at each latitude in the cross-shore direction between the coast and 200-m isobath is compared to the similarly averaged observed SSH, using a series of the weekly AVISO (www.aviso.altimetry.fr) absolute dynamic topography maps obtained by interpolation from several altimeters (Fig. 5). The model SSH has a higher temporal resolution (daily vs. weekly) and a higher spatial resolution (2 km vs. one-fourth degree) than the gridded altimetry. It shows frequent alongshore coherent events associated with the northward propagation of coastally trapped waves. Qualitatively consistent with the observed SSH, model SSH fluctuations are generally positive (higher) during the season of

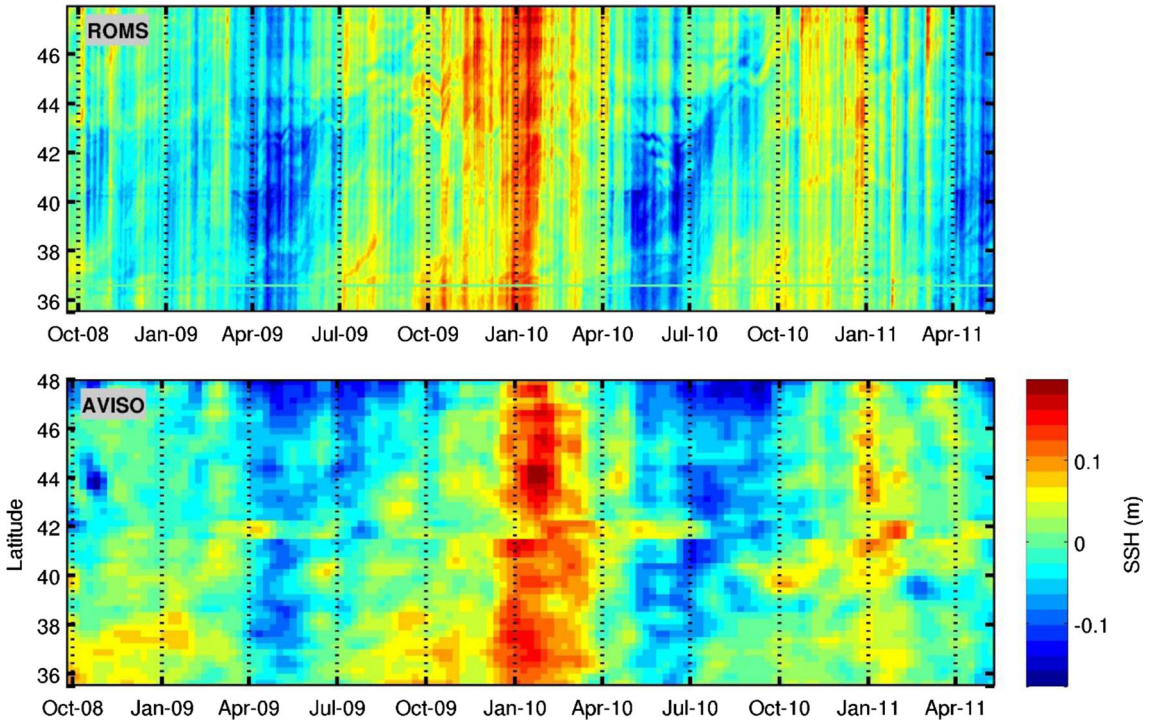

Fig. 5 (*Top*) Model and (*bottom*) observed (AVISO absolute dynamic topography maps) SSH averaged between the coast and the 200-m isobath and presented as a function of time and latitude

predominantly downwelling-favorable winds (October through March) and negative (lower) during the season of upwelling-favorable winds (April through September) (Fig. 4). The inter-annual variability is also visible as the SSH is higher all along the coast during the period of peak positive MEI (winter 2009–2010), compared to the previous and following winters.

To compare variability in the sea surface temperature (SST) along the entire coast, we utilize the operational SST and sea

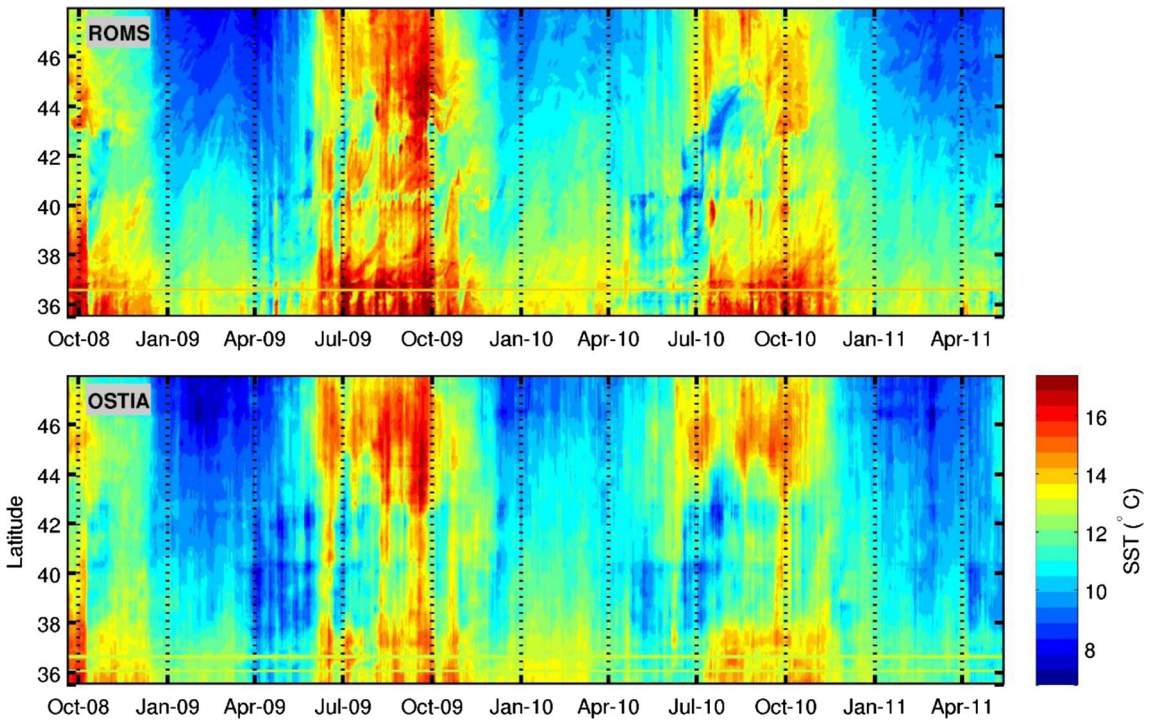

Fig. 6 (*Top*) model and (*bottom*) observed (OSTIA) SST averaged between the coast and the 200-m isobath and presented as a function of time and latitude

ice analysis (OSTIA) product, based on synthesis of data from several satellites and in situ data (Donlon et al. 2012). The modeled and observed SST are averaged along each latitude between the 200-m isobath and the coast and shown as functions of latitude and time (Fig. 6). The model is consistent with observations in representing the annual cycle, with warmer SST roughly June through October and colder SST from December through March, along the entire north-south extent (35 and 50N) of the domain. The winter months however are characterized by a notable north-to-south gradient in SST whereas other seasons show greater alongshore uniformity. The spring transition is marked by particularly strong upwelling winds in the southern portion of the domain (Fig. 4) that brings cold water to the surface on the shelf. This eliminates or even temporarily reverses the N-S SST gradient. Conversely, the autumn-to-winter transition is marked by particularly intense northward winds in the northern portion of the domain (Fig. 4) that likely contributes to reintroducing the N-S SST gradient via enhanced vertical mixing over the northern shelf.

Similar to what was observed for SSH (Fig. 5), the period coinciding with positive MEI (June 2009 through April 2010) exhibits relatively warmer SST compared to the same period in the preceding and following years that coincide with negative ENSO anomalies. Comparing SST in the near-coastal region during winter, the coldest surface temperatures are found in 2008–2009, in which of the three winters, the northward wind forcing was weakest and the surface heat loss was largest.

During the entire study period, high-frequency (HF) radar observations of surface currents off Oregon (Kosro et al. 1997, Kosro 2005, Kim and Kosro 2013, Kim et al. 2014) are available, in the area of 41–46N. Data are provided as daily maps of two orthogonal velocity components (meridional u and zonal v) on a regular 6-km grid. These maps were obtained as a result of objective mapping of radial component data from several standard (50 km) and long-range (150–200 km) radars. The footprint of quality-controlled HF radar data varies daily due to changes in environmental conditions. Model daily surface currents are sampled at locations and times where and when the data are available. The observed and sampled model u and v components are area-averaged for each day and the resulting time series are presented in Fig. 7. Overall, the

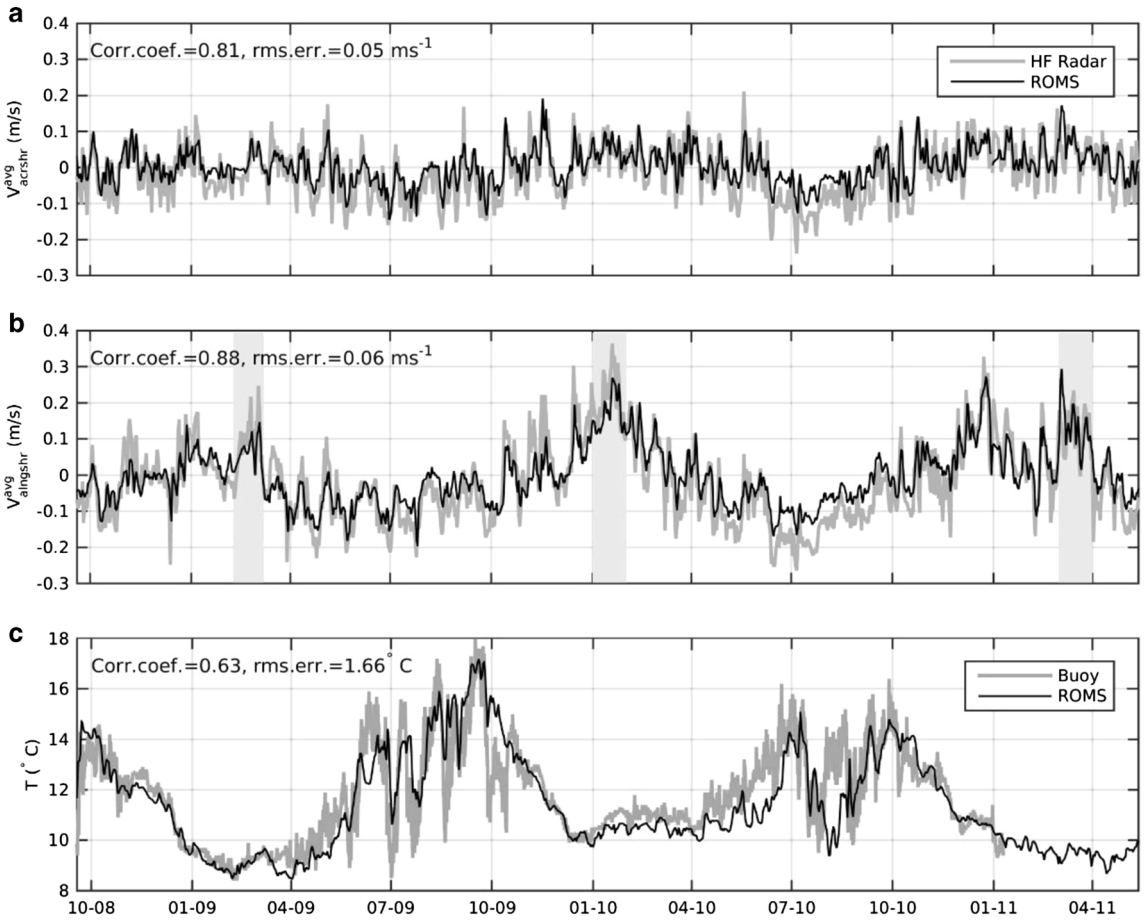

Fig. 7 Time-series of **a** area-averaged surface alongshore and **b** cross-shore velocity off Oregon from HF radar (*gray line*) and model (*black line*), using values sampled at the HF radar observation locations and times, temperature at 2 m below the surface from an observational mooring (NH10—*gray line*) and **c** surface model temperature (*black line*). *Gray-shaded boxes* in **b** indicate the month in each year with peak northward current

model reproduces qualitatively correctly the variability in the surface alongshore and cross-shore currents on temporal scales of a few days to seasonal. This is true from very near the onset of the simulation, indicating that shelf circulation adjusts quickly following the HYCOM initialization. As expected, both the observed and modeled meridional currents are substantially weaker in winter 2008–2009 than in the other two winters, peaking in mid-February through early March. The peak currents in winter 2009–2010 and in 2010–2011 are similar in magnitude, with the strongest northward currents found in December 2009 through February 2010 and in December 2010 and March 2011.

The near-surface (2-m depth) model temperature compares reasonably well with the data at the mid-shelf NH10 mooring, anchored at the depth of 81 m at 44.65N (Fig. 7c), which suggests that there is little bias in the model atmospheric heat flux forcing. Relatively low temperatures are found in each winter with little variability in surface temperature between January and the start of April. The El Niño winter exhibits the warmest surface temperatures of the three, with average temperatures for January through March 2010 approximately 1.7° warmer than the same period in 2009 and 1° warmer than the same period in 2011.

4.2 Ocean response during winter

The basic response of the coastal ocean off Oregon to winter forcing is to become colder and more strongly mixed. Model comparisons against the glider cross-shore transects over the shelf and slope between 44 and 45N (Oregon coast) suggest that the model correctly reproduces the variability in the depth of the mixed layer, location of the front, and near-surface conditions on seasonal and wind-event temporal scales. In particular, comparisons of observed and model temperature sections in November 2008, 2009, 2010 (before each winter season) and March 2009, 2010, 2011 (at the end of each winter season) (Fig. 8) are shown to demonstrate that (a) the model mixed layer depth is increased over the winter months in qualitative agreement with the observations, (b) following the winter storms, the surface mixed layer depth may be as large as 100 m, and (c) the observed and model near-surface temperature (including the warmer conditions in March 2010) are in agreement. Note that for this comparison, the model section is obtained by sampling the model output at the actual

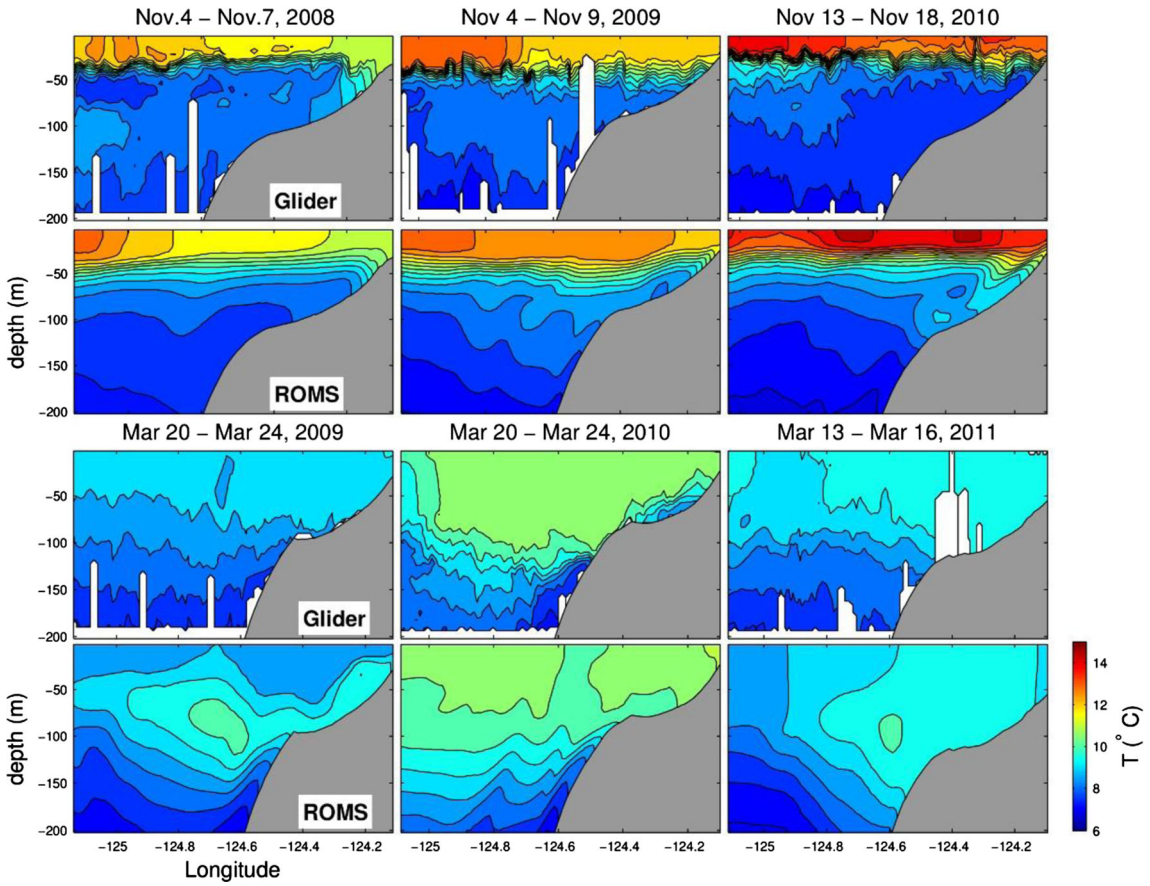

Fig. 8 Glider and model temperature sections near 44.6N, (*top half*) in November before each winter, (*bottom half*) in March following each winter. (*Rows 1* and *3*) glider, (*rows 2* and *4*) model

glider locations and times. It takes about 3 days for the glider to complete sections like those shown. In the sections from March 20 to 24, 2010 (bottom rows, middle column), the glider samples through one of the first upwelling events of the year following a period of intensified northward winds (Fig. 1). The upslope advection of colder water during this time shown in the glider sections is captured by the model.

Similar glider comparisons performed for the salinity fields (Fig. 9) show that the model reproduces deepening of the halocline following each winter qualitatively correctly. At the same time, a positive bias in the near-surface salinity is apparent in years 2 and 3 of the simulation. The HYCOM model used for initial and boundary information assimilates ARGO float temperature and salinity profiles, which helps to constrain the near-surface salinity and apparently results in low bias at the beginning of our simulation. Low-salinity water sources that may contribute to the freshening of the near-surface waters on a regional scale and that are not accounted for in our model include the Columbia River at 46.2N (e.g., MacCready et al. 2009, Hickey et al. 2010), the Fraser River that communicates with the ocean through the Juan de Fuca Strait (48N), Puget Sound that collects fresh water inputs from many small sources and exchanges water mass through Juan de Fuca Strait with every tidal cycle (Sutherland et al. 2011), and possibly precipitation. Also, discharges from small rivers along the Oregon and Washington coasts peak in winter and influence salinity and circulation locally over the shelf near the coast (Mazzini et al. 2014). The impact of these sources to improve the representation of the salinity signal in our study area will be a subject of future studies.

In winter 2010–2011, the warm water anomaly along the coast in the Pacific Northwest (Fig. 6), found also at the glider and buoy positions (Figs. 7 and 8), presumably resulted from both the positive anomaly in the heat flux over the preceding summer seasons (Fig. 2) and advection of warmer waters by intensified northward currents. The spatial structure of this anomaly at the sea surface is visible in weekly averaged SST from satellite (OSTIA) and the model at the end of winter at approximately the same time as the March glider observations (Fig. 10). A tongue of warmer SST is identified along the coast by this time in 2010 in the satellite data, in contrast to the preceding and following years. The model nicely reproduces this effect and resolves a complex eddying structure

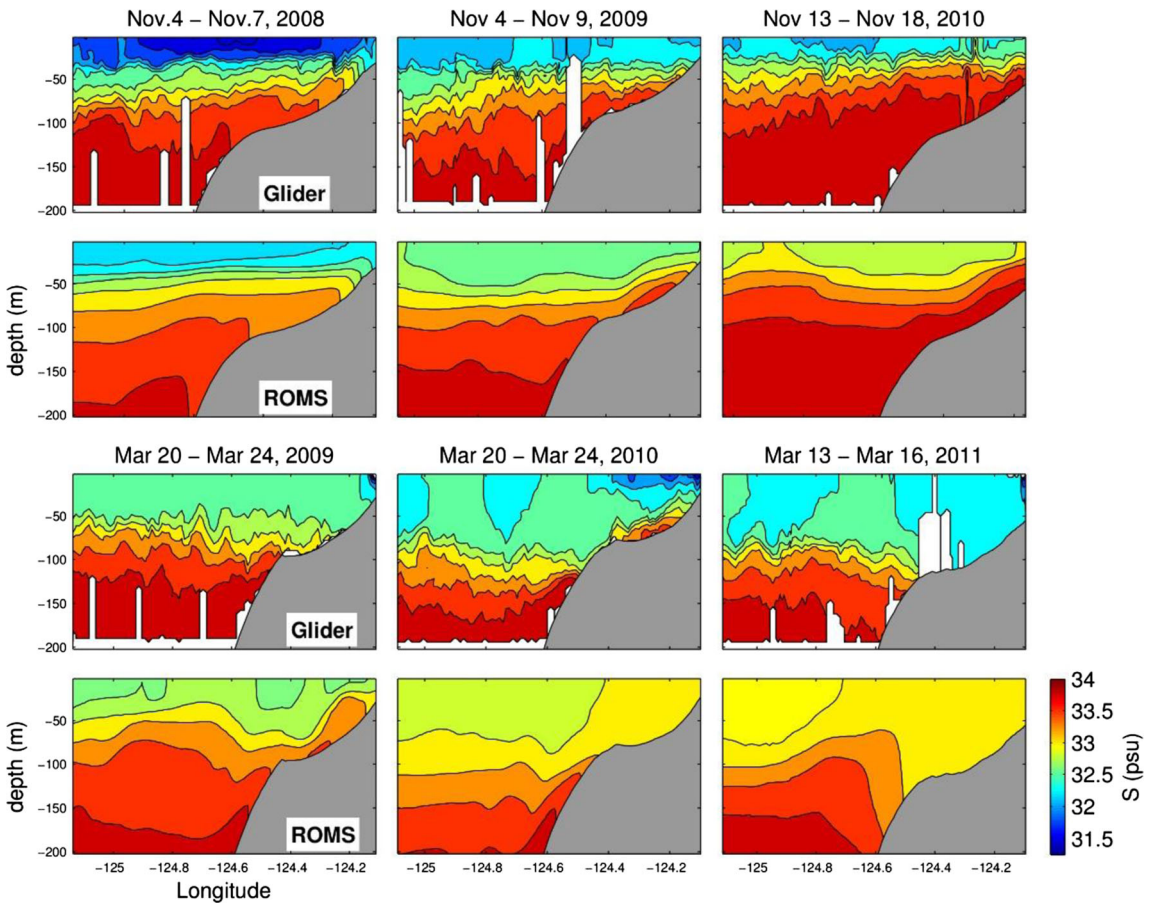

Fig. 9 Glider and model salinity sections near 44.6N, (*top half*) in November before each winter, (*bottom half*) in March following each winter. (*Rows 1* and *3*) glider, (*rows 2* and *4*) model

associated with it, reinforcing the case that advection is playing a role in its development.

4.3 Peak downwelling months

To further elucidate the role of advection in determining Oregon shelf characteristics during the winter season, we examine currents during periods of peak downwelling conditions in each of the three winters. We identify these as month-long periods with the strongest positive meridional current as observed in the area-averaged HF radar data for the Oregon shelf. These are February 8–March 8 2009, January 1–31, 2010, and March 1–31, 2011 (indicated as shaded periods in Fig. 7b) (March 2011 is chosen over December 2010 for the third winter, as it better represents the fully developed winter season conditions). Model-derived current fields compare well qualitatively to maps of HF radar surface currents averaged over these periods (Fig. 11). In both the model and observations, intensified northward surface currents extend offshore of the 200-m isobath over the continental slope and appear to be roughly constrained by bathymetric contours. The modeled downwelling jet is comparable to the radar observations in 2009, less diffuse than the observations in 2010, and centered moderately farther offshore in 2011. Quantitatively, the model correlates best with the HF radar surface currents shoreward of approximately the 250-m isobath during the winter seasons as measured by the magnitude of the complex correlation coefficient (Fig. 12). Root-mean-square error between modeled and observed fields is largest nearshore north of Cape Blanco.

The structure of these surface currents in the model on a larger alongshore scale is presented in Fig. 13. In peak months, the northward flowing current can be traced down the coast as far as 36N. Interaction with oceanic eddies appears to influence the continuity of the current, particularly when the current is stronger and centered farther offshore. North of 41N, the currents are generally strongest in January 2010, with those in March 2011 also comparatively strong and those in February 2009 considerably weaker.

The vertical structure of the alongshore downwelling jet reveals that it is a relatively deep feature, greater than 150 m in depth, that may be surface or subsurface intensified at different times and at different positions along the coast (Fig. 14). Cross-shore sections of potential density (also displayed in Fig. 14) show that at 44.6N, out to about 100 m depth, the waters are mixed from surface to bottom on average over each peak month in 2010 and 2011, but not in 2009. The vertical shear in the horizontal current along the shelf break at 44.6N is qualitatively in thermal-wind balance with the strong horizontal cross-shore density front separating relatively well-mixed surface/shelf waters and the stratified interior. In cross-shore zonal sections farther south at 42N, where the shelf is much narrower, the shelf volume is likewise well-mixed out to the 100-m isobath in all 3 years. At 39N, where the shelf slopes downward steeply from very near the coast, the weaker downwelling jet in 2009 is farther offshore, and the near coast

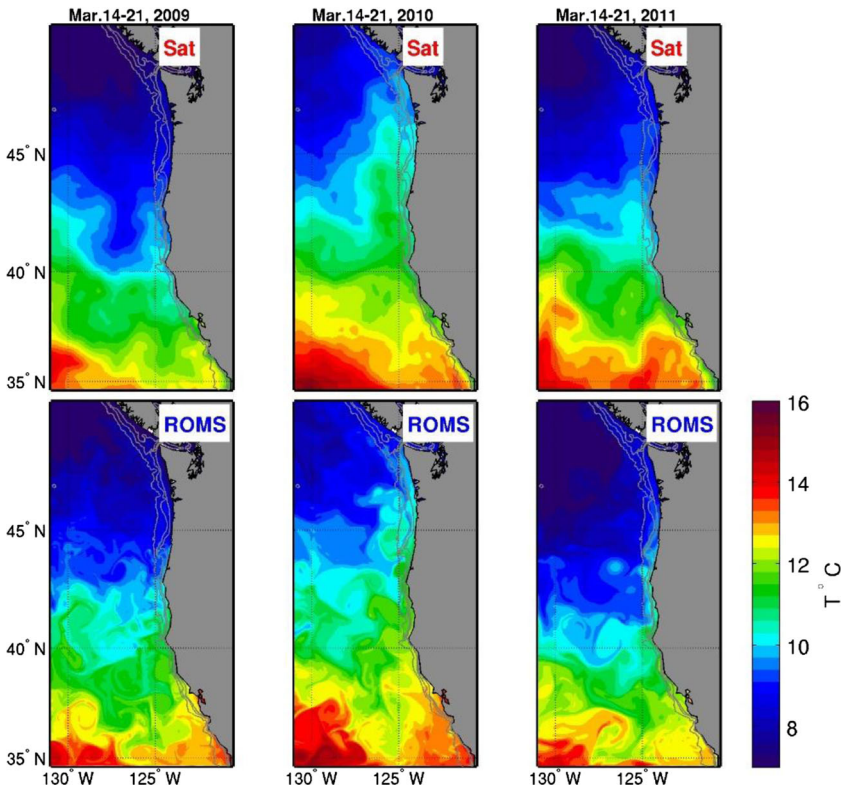

Fig. 10 Average SST in the second week of March (*left* to *right*): 2009, 2010, and 2011. (*Top*) the operational sea surface temperature and sea ice analysis (OSTIA) satellite product, (*bottom*) model

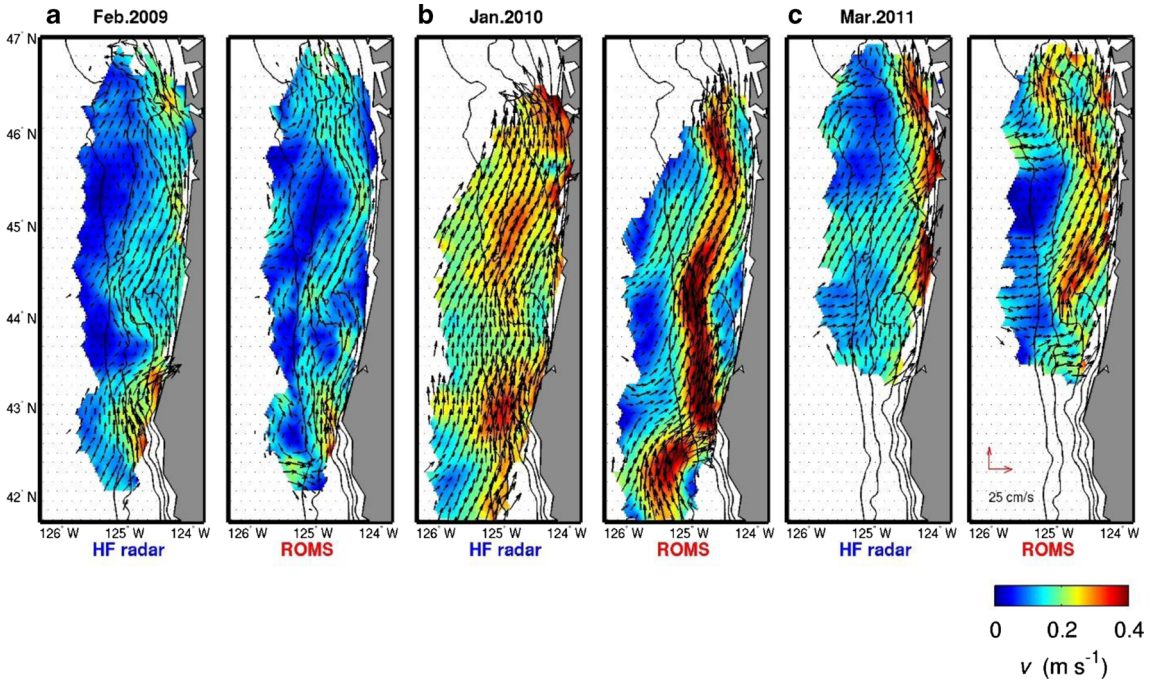

Fig. 11 Surface currents off Oregon from HF radar and the model averaged over month-long periods of peak northward winter flows (see Fig. 7b): **a** February 8–March 8, 2009; **b** January 2010; **c** March 2011. *Black contour lines* indicate the −2000-, −1000-, −500-, −200-, and −100-m isobaths

environment is more well-mixed than in either 2010 or 2011 (Fig. 14). On the offshore side of the jet, the isopycnals slope downward in the offshore direction in both 2010 and 2011, which in conjunction with the surface currents (Fig. 13) suggest that oceanic eddies or currents may be limiting the offshore expression of the coastal downwelling circulation at this location and time.

The northward coastal current in January 2010 is found to separate from the narrow shelf between Cape Mendocino and Cape Blanco (40–42N) (Fig. 13). A pattern similar to this was

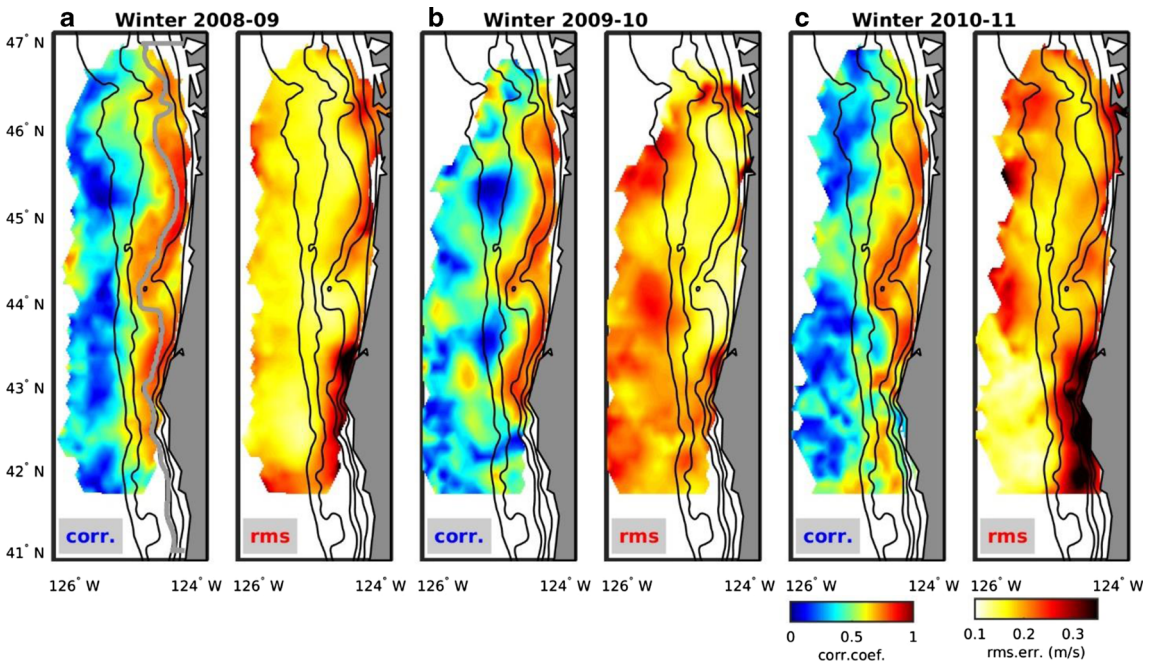

Fig. 12 Magnitude of the complex correlation coefficient and root-mean-square error between HF radar observations of surface velocity and model surface fields for the three winters (DJFM). *Black contour lines* indicate the 2000-, 1000-, 500-, 200-, and 100-m isobaths. The *gray line* in the *leftmost panel* indicates the boundary of the coastal control volume discussed in Section 5

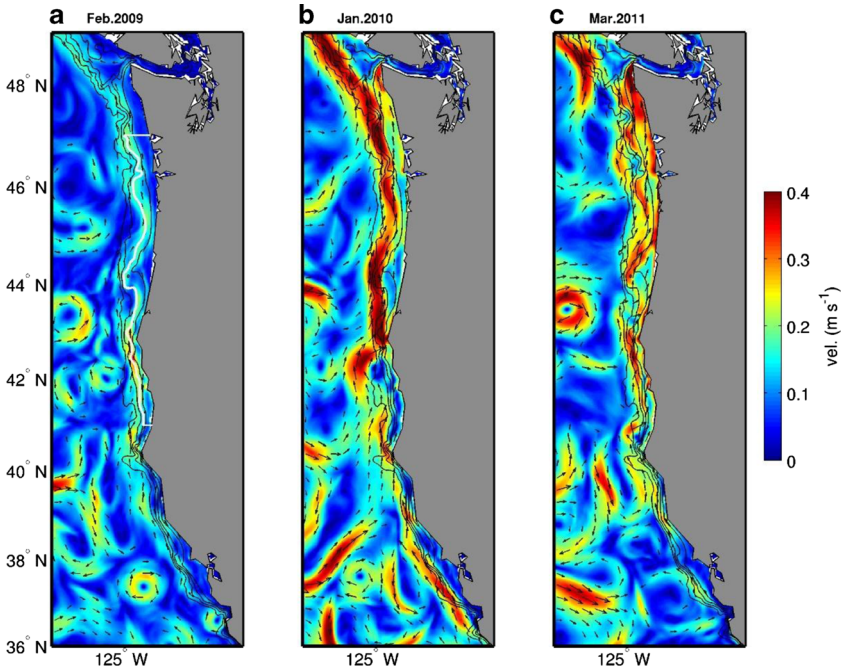

Fig. 13 Monthly averaged alongshore surface current magnitude (*color*) and direction (*vectors*), 38–50N, during peak winter months in each winter. *Black contour lines* indicate the depths of the 1000-, 500-, 200-, and 100-m isobaths. *White lines* in (**a**) delineate the coastal control volume referred to in Section 5

also found by Bjorkstedt et al. (2010) in analysis of winter-averaged HF radar data for the same year (see their Fig. 8d). The results of this separation are also shown in the cross-shore *v*-section at 42N (Fig. 14), where the maximum of the January 2010 northward jet is found considerably farther offshore than the shelf break.

Given the increased intensity of the northward flow along the shelf and slope in winter 2009–2010, compared to 2008–09, we initially hypothesized that the advection of waters from California would result in anomalously warmer and saltier waters along the shelf break farther north in spring 2010. These waters would be available for upwelling in Oregon, causing an anomaly in the near-bottom waters over the shelf in summer. However, analyses of available glider and mooring observations (Adams et al. 2013) show that the temperature-salinity properties near the bottom over the Oregon shelf in

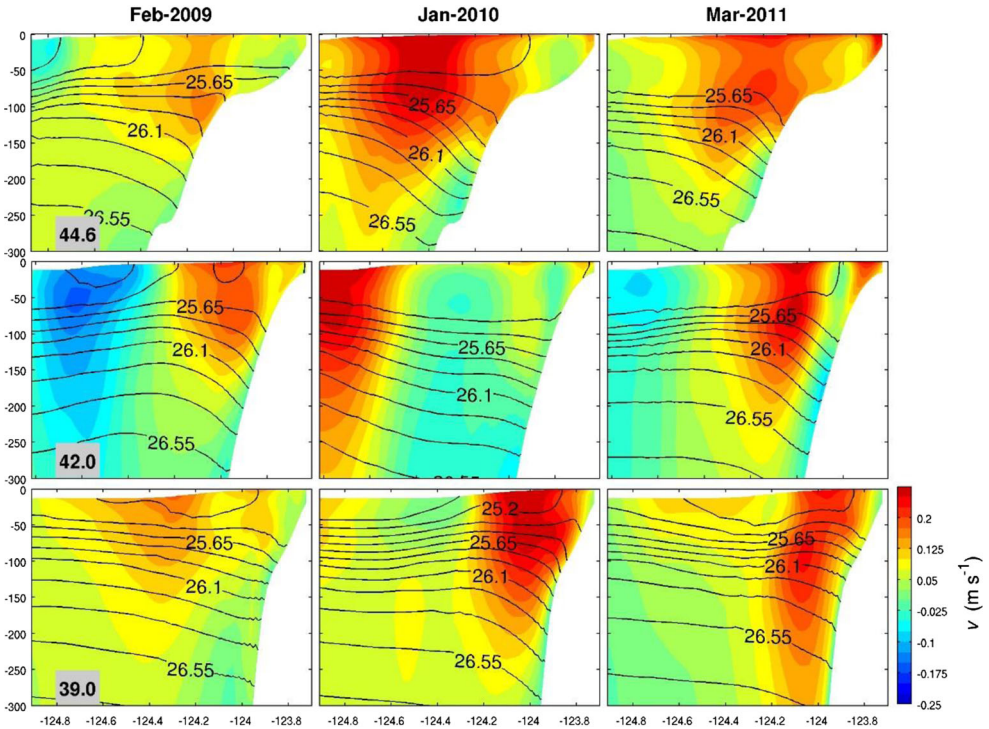

Fig. 14 Vertical cross-sections of the monthly averaged meridional current component (*color*) and potential density anomaly (*lines*), during peak winter months for each year

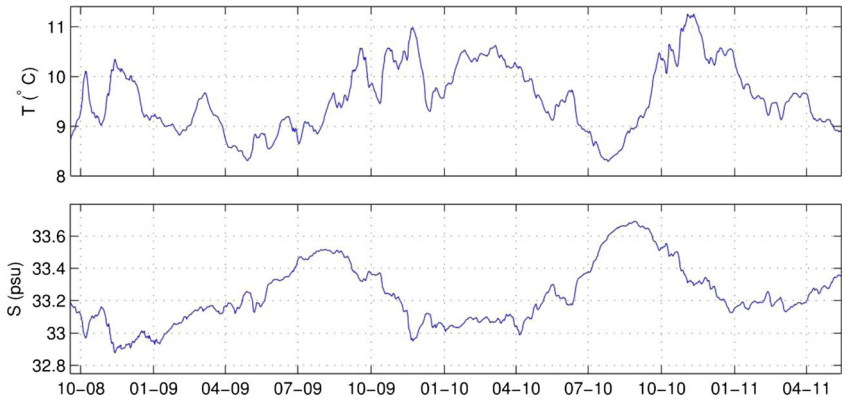

Fig. 15 Volume-averaged temperature (*top*) and salinity (*bottom*) in the coastal control volume (CV) between 41 and 47N and inshore of the 200-m isobath

summer 2010 were close to average, and our model results are consistent with this. Additional analyses of model results (not shown) revealed intense eddy variability over the slope, including subsurface intensified eddies (at the scales on the order of 50 km), in winter 2009–2010 that may have contributed to offshore transport of the heat and salt during that time period. The mechanisms for eddy generation and estimates of the momentum, heat, and salinity fluxes associated with eddies over the slope and in the adjacent interior ocean will be addressed in future studies.

5 Volume-integrated heat and salinity over the shelf

The available solution allows an assessment of the seasonal variability in the average heat and salinity content over the shelf and an analysis of the interannual variability over the 32-month period. Accordingly, the model potential temperature (T) and salinity (S) are integrated in a coastal control volume (CV), south to north between latitudes 41 and 47N, west to east from the 200-m isobath to the coast (Fig. 13a), and in the vertical from the bottom to the surface. This coastal control volume includes all of the Oregon and part of the Washington shelf where intense coastal upwelling is observed in summer and strong downwelling is found in winter. The choice of the alongshore extent was partly motivated by our earlier study (Kurapov et al. 2011), where the volume-integrated heat balance was analyzed for a similar region, but only for a part of a summer upwelling season. Here, we have a chance to complete the seasonal cycle, assess the behavior during winter, and address interannual differences.

The volume-averaged T and S in the coastal CV as functions of time are shown in Fig. 15 where interannual, annual, and shorter-term variabilities are visible. The characteristics of this time variability are analyzed and discussed below. To assist in the interpretation of that variability, the cumulative north-south surface wind stress averaged over the CV ocean surface and the cumulative CV volume-averaged north-south velocity are shown in Fig. 16. The annual cycle in the wind stress, negative (southward, upwelling-favorable) in summer from about April to September and positive (northward, downwelling-favorable) in winter from October to March, is evident from the negative and positive slopes, respectively, in the cumulative stress curve. The northward winter wind

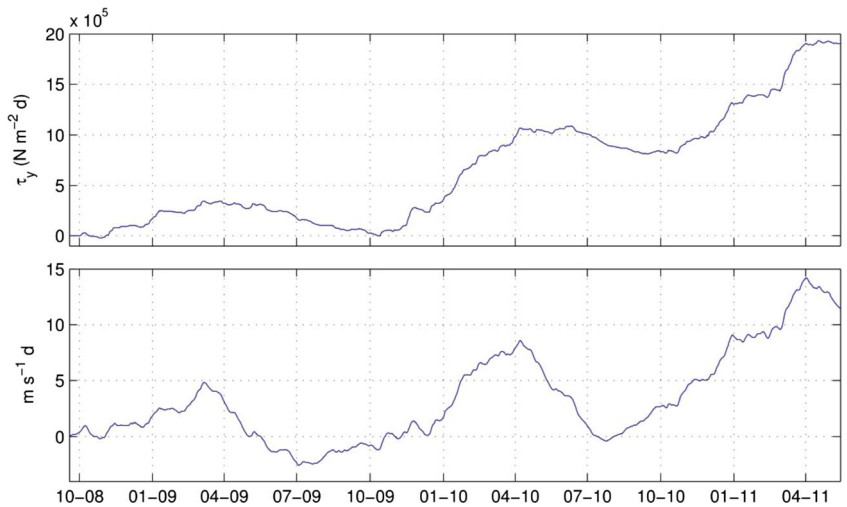

Fig. 16 (*Top*) The cumulative north-south wind stress averaged over the CV surface area and (*bottom*) the cumulative CV volume-averaged north-south velocity

stresses in 2009–2010 and 2010–2011 are considerably stronger than in winter 2008–2009 and also considerably stronger than the summer southward wind stresses in 2009 and 2010. Periods where the cumulative stress levels off on the seasonal scale delineate periods of seasonal spatial and/or temporal variability in the prevailing wind direction over the coastal control volume. For example, the cumulative northward wind stress is rather flat between April and the middle of June 2010 despite this generally being considered the upwelling season on the US West Coast. During this time, although winds are predominantly southward, there are intermittent wind reversals to northward, particularly in the northern portion of the control volume (Fig. 4). Peak upwelling-favorable winds during this period tend to be centered to the south of the Oregon-Washington coastal control volume.

The variability of the volume-averaged north-south velocity is related to that of the wind stress. It is generally southward in summer and northward in winter, but with the velocities southward only from about April to July and northward the rest of the year, from about August to April. The northward velocities found during August–September evidently reflect the influence in the CV-average of the northward current fluctuations south of about 43N, shown for the surface currents in Fig. 4 and observed in current measurements at 42.44N during 2000–2003 by Ramp and Bahr (2008). Similarly, the strong CV-averaged cumulative southward currents between April and June of 2009 and 2010 evidently reflect not only local winds but also the influence through coastal-trapped wave dynamics (e.g., Denbo and Allen 1987) of the strong upwelling-favorable winds that have developed most strongly to the south of the CV during this period.

The temporal variability in the volume-integrated heat content (Fig. 15) is primarily a result of the imbalance between the area-integrated atmospheric heat flux and the advective heat flux through the lateral boundaries. Cumulative time integrals in these three terms are shown in Fig. 17, normalized appropriately by the volume, water density, and specific heat to show change in units of degrees Celsius and offset by the value of the volume-averaged temperature at the beginning of the analysis time interval. Variations in the volume-average temperature are smaller than in the boundary heat flux terms, which tend to have opposite signs. On the interannual time scale, the atmospheric heat flux tends to warm the volume, and this is balanced on average by an outward advective heat flux through the open boundaries. The atmospheric heat flux integral has local minima in March of each year (at times where winter cooling through the ocean surface is turning to warming in spring). This heat flux warms the volume by about 4 °C between April 2009 and March 2010 (El Niño season), compared with about 1.5 °C between April 2010 and March 2011. This is counteracted by the advection of heat out of the domain, tending to cool the control volume by about 3.5 °C between March 2009 and March 2010 and 2 °C between March 2010 and March 2011. A result of those differences is that the volume-averaged temperature in March 2010 is about 0.5 °C warmer than in March of the preceding or following year.

In the annual cycle of volume-averaged T (Fig. 15), the maximum value in each model year is reached in November, about a month after advective cooling associated with upwelling switches to advective heating associated with downwelling and after the atmospheric heat flux changes the other way from summer heating to winter cooling (Fig. 17). The maximum value is around 11 °C in both 2009 and 2010. The minimum is found in summer, in May during 2009 and in July during 2010. That difference in timing evidently corresponds to the earlier seasonal shift to persistent southward upwelling-favorable winds in April 2009 compared to about June 2010 (Figs. 4 and 16).

It is helpful in trying to better understand the variability of the CV volume-averaged temperature to assess the time-dependent behavior of the atmospheric heat flux integrated over the CV ocean surface (Fig. 18). The net positive heat flux in summer 2009 (April–September) is notably larger than in summer 2010, primarily due to greater shortwave radiation in summer 2009. A similar result was found for the net flux over the whole domain (Fig. 2). Between October and March, the net fluxes are negative, as a result of reduced shortwave radiation and increased negative latent cooling. The time variability of the negative net fluxes in winter generally follows that of the latent and sensible fluxes. There is notably more cooling in January–March of 2011 than there is in the same months in either 2009 or 2010.

Conditions at the offshore 200-m isobath western boundary of the *CV*, that contribute to the seasonal differences in the heat and salinity fluxes and in particular to the differences during the three winters, may be assessed by computing the vertical profiles of temperature, salinity, and N^2, averaged horizontally along the 200-m isobath (between 41 and 47N) and plotted as a function of time (Fig. 19). The annual cycle in stratification over the 200-m isobath, stronger in April through September during summer upwelling and weaker in October–March during winter downwelling, is shown by all the variables, but is especially clear in the salinity and N^2 plots. In particular, the sharp reductions in the stratification in January 2010 and, to a somewhat less extent, in December 2010 and March 2011, coincident with the strong northward wind stress in those months (Fig. 16), are evident. The temperature profiles show generally warmer water during January through March of the 2010 El Niño winter than in the same winter months in 2009 and 2011.

To better understand the nature of the total advective heat and salinity fluxes into the CV, we calculate, in a manner explained below, the time-dependent cumulative fluxes through the three separate boundaries, northern (47N), southern (41N), and western (200-m isobath). Before doing that, it

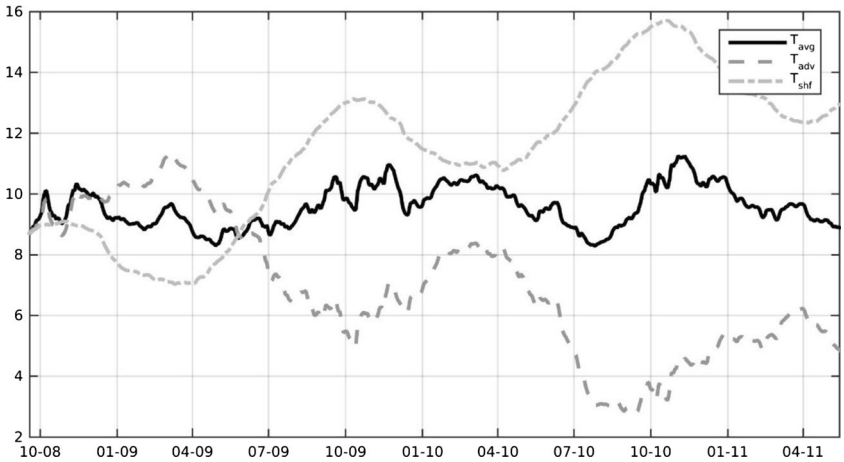

Fig. 17 The cumulative terms in the CV volume-averaged temperature equation; averaged temperature (*thick black*), accumulated atmospheric heat flux into the volume (*gray, closely-spaced dashes*; the increasing function means warming the volume-averaged temperature) and the heat flux advected through the ocean boundaries (*gray, widely-spaced dashes*; southern, northern, and western boundaries combined)

is useful to assess the cumulative volume fluxes through those boundaries (Fig. 20). Those fluxes sum to near zero values with a small residual that we will neglect in the following discussion. That approximation corresponds, in the volume integral of the continuity equation, to a neglect of the contribution from the surface area integral of the time derivative of the sea surface height relative to the contributions from volume fluxes through individual separate boundaries. The resultant relative error may be quantified by a calculation of the root-mean-square value of the sum of the volume fluxes through the separate boundaries divided by the root-mean-square value of, e.g., the western boundary flux. That calculation gives 0.013, which is indeed small. It may be seen that, for this CV, the dominant boundary fluxes are through the western and northern boundaries. At the western boundary, the volume flux is generally positive into the CV during winter from about October to March, being relatively strong in winters 2009–2010 and 2010–2011. Negative fluxes out of the CV are found in summer from April to September. These winter and summer seasons correspond approximately to those of the wind stress (Fig. 16). The western boundary volume flux is primarily balanced by that at the northern boundary, which is negative (northward) out of the CV in winter and positive (southward) into the CV in summer, in general agreement with the behavior of the cumulative volume-averaged alongshore velocity (Fig. 16). The flux at the southern boundary is negative (southward) out of the CV in April through about June and weakly positive (northward) most of the rest of the year. The volume fluxes in Fig. 20 are normalized by the total volume of the coastal CV so that a change in cumulative normalized transport equal to ±1 represents the time it takes for the volume fluxed through a boundary to equal the entire contents of the CV. The volume renewal time scale is about 3 months during

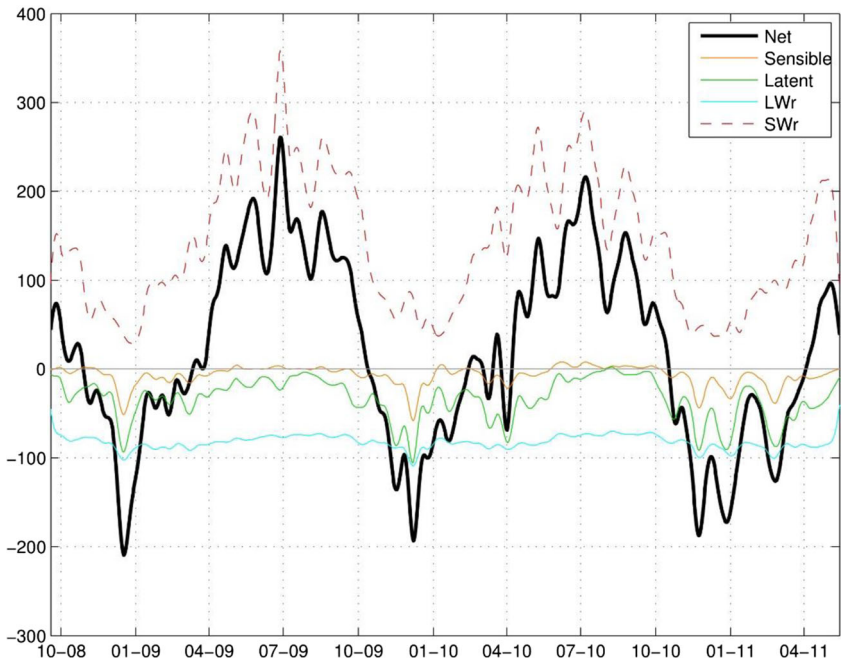

Fig. 18 Time-series of the net atmospheric heat flux, together with the components, integrated over the surface of the CV after application of a 30-day filter. The heat flux components are shortwave radiation, longwave radiation, latent, and sensible

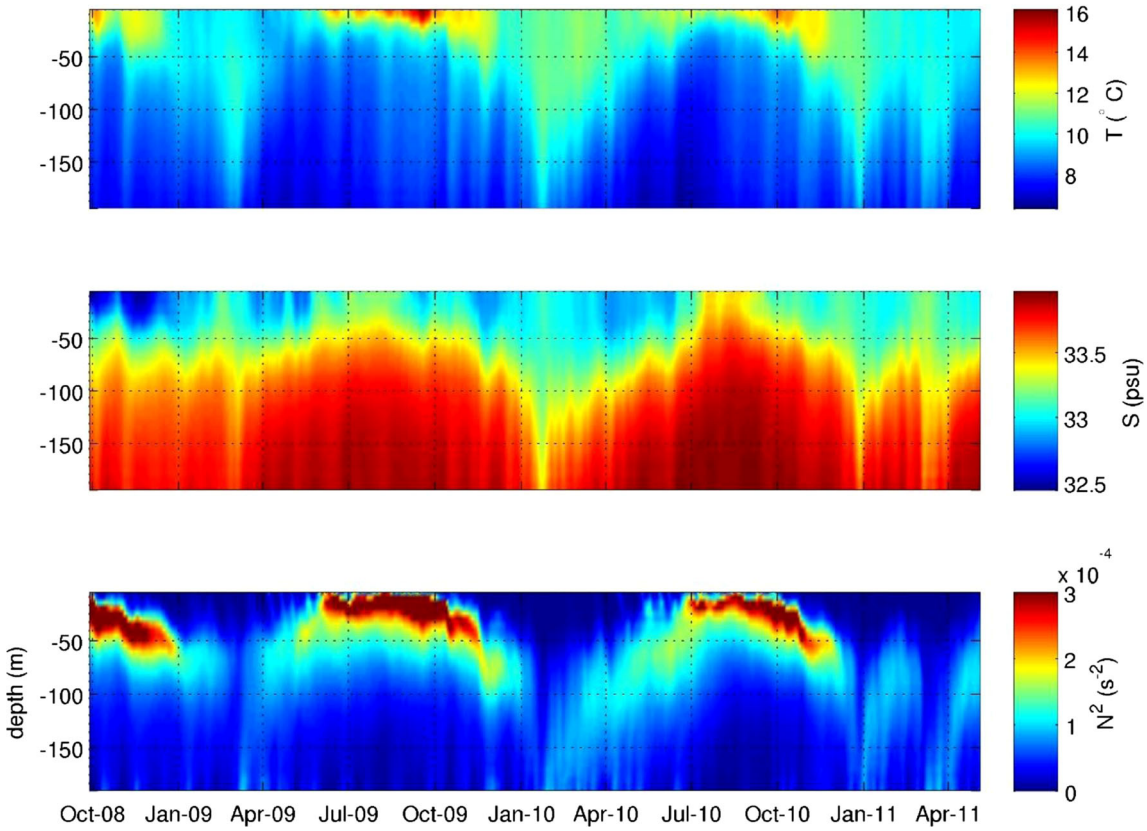

Fig. 19 Vertical profiles of temperature, salinity, and N^2 averaged horizontally along the 200-m isobath at the CV western boundary plotted as a function of time

upwelling conditions and is much faster, near 1 month, in winter downwelling conditions.

The heat fluxes through the separate boundaries are calculated by using, in the heat flux calculation, $u_n(T - T_{\mathrm{ref}}) = u_n(T - T_{\mathrm{avg}}(t))$, where $T_{\mathrm{avg}}(t)$ is the time-dependent volume-averaged temperature and u_n is an appropriate normal velocity (Lee et al. 2004). In that way (assuming for this argument that the normal velocity is positive into the CV), every local flux that is positive (negative) may be interpreted as increasing (decreasing) $T_{\mathrm{avg}}(t)$. In the continuity equation, again neglecting the relatively small contribution from the time derivative of the sea surface height, we found the volume fluxes

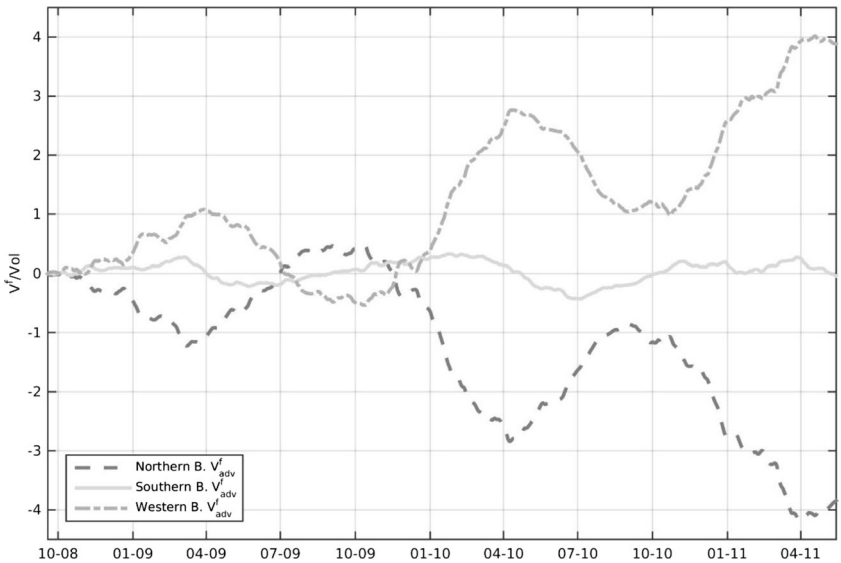

Fig. 20 Cumulative volume flux terms for the separate boundaries of the CV, western (200-m isobath), northern (47N), and southern (41N). Since volume is conserved, these separate boundary fluxes balance and effectively sum to zero (see text)

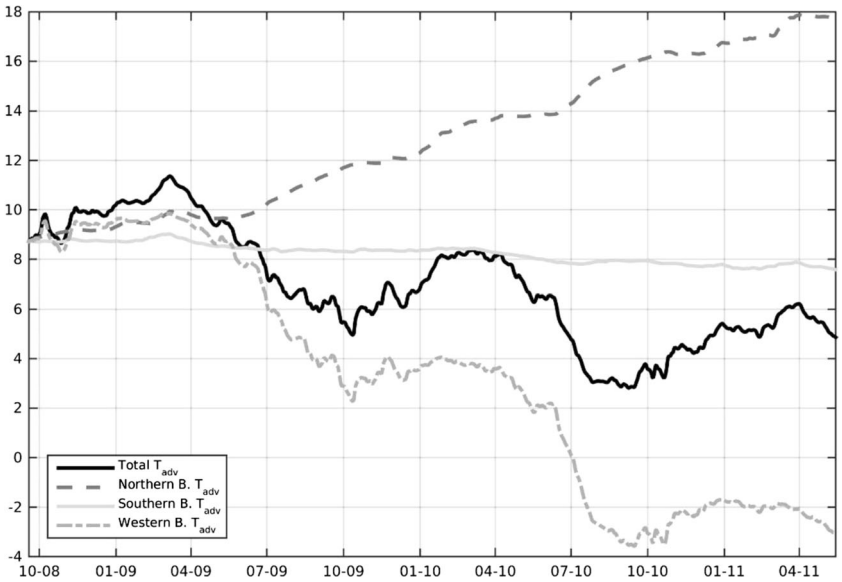

Fig. 21 Cumulative advective heat flux terms for the separate boundaries of the CV, western (200-m isobath), northern (47-N), and southern (41-N), calculated as explained in the text, plus the total advective flux from all three boundaries

to be approximately balanced. Consequently, since $T_{ref} = T_{avg}(t)$ is constant in space, this procedure removes from the local fluxes a component that for the separate boundaries may be sizeable but that contributes negligibly to a change in $T_{avg}(t)$ since it represents the advection of a spatially constant $T_{avg}(t)$ by a nearly conserved volume flux (Fig. 20). As a check, we find numerically that the sum of the separate boundary fluxes is a very close approximation to the total advective heat flux (Fig. 17) that is calculated based directly on an integration of the model formulation for the advection terms in the equation for T. In this case, the root-mean-square error of the difference divided by the root-mean-square value of the model total advective flux is 0.036, which is again small.

The resulting cumulative separate boundary advective heat fluxes are shown in Fig. 21 along with the total advective flux. It can be seen that the seasonal time variability in the total advective flux is effectively dominated by that of the western boundary flux. By a comparison of the variability of the wind stress (Fig. 16) with that of the western boundary heat flux, a general relationship may be seen between northward downwelling-favorable wind stresses and positive warming fluxes during approximately October through March and the opposite, between southward upwelling-favorable wind stresses and negative cooling fluxes during April through September. The 2-year trend (April 2009–March 2011) of the western boundary cumulative heat flux (Fig. 21) is negative, which reflects the fact that, at the western boundary, the cooling advective fluxes, associated with southward upwelling-favorable winds in summer, are more effective in changing the volume-averaged temperature than are the heating fluxes associated with the northward downwelling-favorable winds in winter. It is notable that this occurs in spite of the fact that during the 2-year period (April 2009–March 2010), the northward winter winds are considerably stronger, as illustrated by the positive 2-year trend of the cumulative wind stress (Fig. 16) and correspondingly, the cumulative western boundary volume flux is larger in winter than in summer (Fig. 20). As indicated by the plateau-like behavior in the cumulative western boundary heat flux during January–March of both 2010 and 2011, the positive cooling fluxes during early winter decrease to relatively small values during those peak wind winter months. That behavior is evidently associated with the displacement offshore of stratified water by downwelling circulation processes between 41N and 47N, leaving relatively less stratified water inshore of the 200-m isobath (Figs. 14 and 19) and correspondingly decreasing $T - T_{avg}(t)$ on the boundaries, thus weakening the net across-isobath heat flux. It appears to be that process, a counterpart of which is not found in the upwelling circulation, that limits the effectiveness of the downwelling circulation in warming the water inshore of the 200-m isobath in the presence of strong downwelling-favorable winds later in the winter.

The northern boundary heat flux has a positive (heating) 2-year trend (April 2009–March 2011) that tends to partly balance the corresponding negative trend of the western boundary heat flux. The positive fluxes at the northern boundary are present in both summer (July–September) and winter (January–March) and are evidently determined by the southward flux of relatively warm water into the CV during summer upwelling and the northward flux of relatively cold water out of the CV during winter downwelling. At the southern boundary, the 2-year trend is negative and considerably smaller than that from either the northern or western boundaries (partly because the area of the southern boundary, over a narrow part of the shelf, is much smaller than the other two). Contributions to the southern boundary negative trend occur during the April–June time periods by the southward

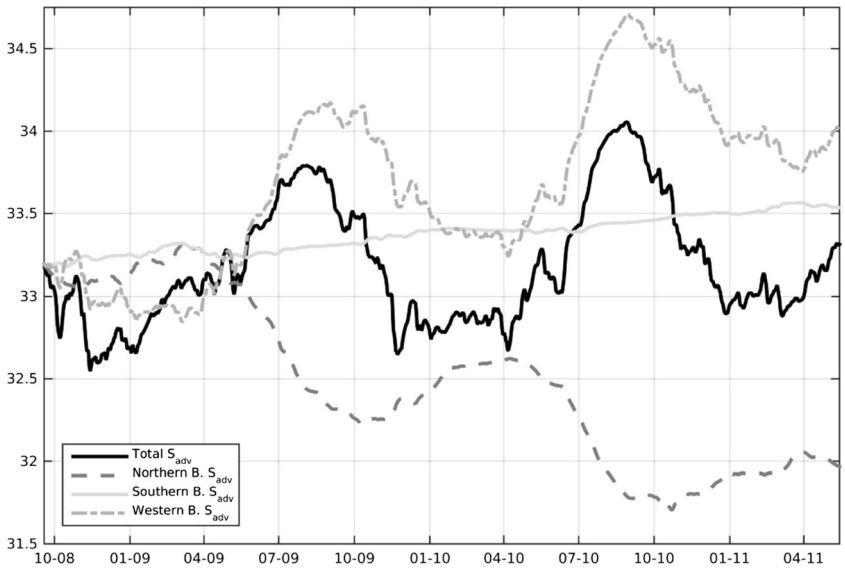

Fig. 22 Cumulative advective salinity flux terms for the separate boundaries of the CV, western (200-m isobath), northern (47N), and southern (41N), calculated as explained in the text, plus the total advective flux from all three boundaries

advection (Fig. 16) of relatively high T water out of the CV. There are relatively weak positive fluxes during the months of exceptionally strong northward winds and strong northward currents February 2009, January 2010, and March 2011. The weak negative or near zero fluxes during July–October, time periods when the volume fluxes are generally northward into the CV, appear to result from an intensification of the northward flow in the lower part of the water column (not shown), a qualitative feature that is consistent with observations (Ramp and Bahr 2008) at 42.44N during "autumn" in 2000–2003. Overall, the negative 2-year trends (April 2009–March 2011) in the western and southern boundary heat fluxes dominate the positive trend in the northern boundary flux and result in the negative trend in the total advective heat flux (Fig. 21).

It is likewise useful to examine the time-dependent behavior of the cumulative salinity fluxes through each boundary, calculated in a similar manner and with similar assumptions by using $u_n(S - S_{\mathrm{avg}}(t))$ in the flux calculations. Those are shown in Fig. 22 along with the total advective salinity flux. It may be seen from a comparison of the time-variability of the total flux and the different boundary fluxes that, similar to the situation with the temperature fluxes, the seasonal variability of the salinity flux at the western boundary tends to dominate the seasonal variability of the total advective salinity flux. In addition, a relation between the seasonal variation of western boundary salinity flux and that of the wind stress, qualitatively similar to that found in temperature, is evident. Positive fluxes that increase $S_{\mathrm{avg}}(t)$ occur during approximately April–August, when the wind stress is southward (upwelling-favorable), while negative fluxes that decrease $S_{\mathrm{avg}}(t)$ occur during October–December when the wind stress is positive (downwelling-favorable). Relatively small fluxes are found during the high wind winter months January–March. That behavior is similar to that found in the western boundary heat flux, evidently for the same reason (Fig. 19). As a result, the 2-year (April 2009–March 2011) trend in the cumulative western boundary salinity flux is positive, generally dominated by the positive fluxes during summer (April–September), similar to the behavior of the western boundary heat flux.

The salinity fluxes at the southern and northern boundaries show a different behavior than the corresponding temperature fluxes. One contributing factor to that difference is that there is a persistent tendency for the salinity in the north to be lower than that in the south, so the sign of the northern and southern boundary salinity fluxes are generally consistent with that general gradient and the sign of the corresponding volume fluxes. At the southern boundary, there is a fairly persistent positive salinity flux with weak negative fluxes typically only in March and April, which is the time of relatively strong southward currents at that location (Figs. 4 and 16). At the northern boundary, negative fluxes from about April to September, corresponding to the advection of relatively low S water southward into the CV, are generally stronger than the positive fluxes during October–March, associated with the advection of relatively low S water northward. The relatively large negative trend from the northern boundary salinity fluxes during summer tend to balance on an annual basis the positive trends from the western and southern boundaries. That balance results in a reasonably stable annual cycle in the total advective salinity flux (Fig. 22) and thus in the volume-averaged salinity (Fig. 15).

The volume-averaged temperature varies differently in winter 2009–2010 (El Niño), compared to the previous and following winters (Fig. 15). The volume-averaged T reaches similar maximum values around 11 °C in November 2009 and 2010, while in November 2008, it is closer to 10 °C. For most of the months January–March 2010, however, it is elevated and nearly constant at about 10.5 °C, which is considerably warmer than during those months in 2009 (9 °C) and 2011 (9.5 °C). Similarly, volume-average S is approximately level

at relatively low values during the same 3 months. The plateau-like behavior in temperature during much of the winter 2010 is also exhibited by similar plateau-like behavior in the contributions from the atmospheric heat flux and the total advective flux (Fig. 17). The level behavior in the atmospheric contribution is due to the relatively smaller net flux in winter (Fig. 18). The level behavior in the net advective flux, as discussed above, appears to be related to the coastal ocean response to strong downwelling winds which result in decreased stratification over the shelf (Fig. 19). Similar shelf flow processes seem to be responsible for the corresponding weakening of the advective salinity fluxes during January–March 2010 and the resultant approximately level behavior of the volume-averaged salinity during that time period. The difference in the behavior of the volume-averaged temperature during January–March 2010, compared to the same months in 2009 and 2011, appears to result from the combined strong wind stresses and relatively higher heat fluxes found in 2010. In January–March 2009, the heat flux is similar to that in 2010 (Fig. 18), but the wind stresses are considerably weaker than in the same months in either 2010 or in 2011 (Fig. 16). The shelf is still partially stratified (see Fig. 14, top-left) such that intensification in the wind stress in February 2009 is associated with appreciably strong changes in the downwelling front location and hence the CV-averaged temperature. During January–March 2011, the downwelling wind stresses are generally strong and comparable to those in 2010, but the heat fluxes (Fig. 18) show notably more atmospheric cooling, contributing to reduction in the CV-averaged temperature over winter 2011.

6 Summary

The ocean circulation model, regional-scale by the size of the domain and coastal-scale by horizontal resolution, has been developed to study the dynamical processes by which the ocean in the interior and that over the continental shelf interact along the coast of the US Pacific Northwest (northern California, Oregon, and Washington). The present study has demonstrated the model skill as verified against satellite SST, SSH, surface currents from HF radars, glider temperature and salinity sections, and mooring temperature measurements. The model correctly describes many aspects of the ocean variability on temporal scales from several days to interannual. The analyses were focused on patterns of winter circulation and in particular on the differences in the 2009–2010 winter influenced by the El Niño event. Compared to winter 2008–2009, the El Niño results in warmer ocean waters along the coast, stronger downwelling-favorable winds, and stronger alongshore (northward) and onshore transports. Although the wind forcing and shelf ocean conditions during the following winter of 2010–2011 were closer to those during winter 2010–2011, notable differences were found off Oregon in the behavior of the shelf CV volume-averaged temperature and salinity during the El Niño winter. From January to March 2010, the variability of these variables exhibited a plateau-like behavior that corresponded to the existence of relatively higher temperatures and lower salinities than found during those winter months in either 2009 or 2011.

Availability of this model solution provides opportunities for many study directions, which will be explored in the future, including the structure of the slope flows in winter and summer, surface and subsurface eddy variability in the coastal transition zone, formation of source waters for upwelling, and response of the upper ocean to winter storms.

Acknowledgements This research was supported by the National Science Foundation (NSF, grants OCE-1030922, OCE-0527168 and OCE-0961999), the National Aeronautics and Space Administration (NASA, grant NNX13AD89G), and the National Oceanic and Atmospheric Administration (NOAA), through the Coastal Ocean Modeling Testbed (COMT) program and the Northwest Association of Networked Ocean Observing Systems (NANOOS), the Regional Association of the national Integrated Ocean Observing System (grant NA11NOS0120036).

References

Adams KA, Barth JA, Chan F (2013:) Temporal variability of near-bottom dissolved oxygen during upwelling off central Oregon, J. Geophys. Res. Oceans, 118, doi:10.1002/jgrc.20361

Allen JS, Newberger PA (1995) Downwelling circulation on the Oregon continental shelf. Part I: response to idealized forcing. J Phys Oceanogr 26:2011–2035

Barth JA, Wheeler PA (2005) Introduction to special section: coastal advances in shelf transport. J Geophys Res 110:C10S01. doi:10.1029/2005JC003124

Bjorkstedt EP, Goericke R, McClatchie S, Weber E, Watson W, Lo N, Peterson P, Emmett B, Peterson J, Durazo R, Gaxiola-Castro G, Chavez F, Pennington JT, Collins CA, Field J, Ralston S, Sakuma K, Bograd S, Schwing F, Xue Y, Sydeman W, Thompson SA, Santora JA, Largier J, Halle C, Morgan S, Kim SY, Merkens J, Hildebrand J, Munger L (2010) State of the California current 2009–2010: regional variation persists through transition from La Niña to El Niño (and back?). Calif Coop Oceanogr Fish Investig Rep 51:39–69

Chassignet EP, Hurlburt HE, Smedstad OM, Halliwell GR, Hogan PJ, Wallcraft AJ, Barailled R, Bleck R (2005) The HYCOM (HYbrid Coordinate Ocean Model) data assimilative system. J Mar Syst 65:60–83. doi:10.1016/j.jmarsys.2005.09.016

Chavez FP, Pennington JT, Castro CG, Ryan JP, Michisaki RP, Schlining B, Walz P, Buck KR, McFadyen A, Collins CA (2002) Biological and chemical consequences of the 1997–1998 El Niño in central California waters. Prog Oceanogr 54:205–232

Chhak K, Di Lorenzo E (2007) Decadal variations in the California current upwelling cells. Geophys Res Lett 34:14. doi:10.1029/2007/gl030203

Denbo DW, Allen JS (1987) Large-scale response to atmospheric forcing of shelf currents and coastal sea level off the west coast of North America: May–July 1981 and 1982. J Geophys Res 92(2):1757–1782

Donlon CJ, Martin M, Stark J, Roberts-Jones J, Fiedler E, Wimmer W (2012) The Operational Sea Surface Temperature and Sea Ice Analysis (OSTIA) system. Remote Sens Environ 116:140–158

Fairall CW, Bradley EF, Rogers P, Edson JB, Young GS (1996) Bulk parameterization of air-sea fluxes for tropical ocean-global atmosphere coupled-ocean atmosphere response experiment. J Geophys Res 101:3747–3764

Hickey B et al (2010) River influences on shelf ecosystems: introduction and synthesis. J Geophys Res 115:C00B17. doi:10.1029/2009JC005452

Huyer A, Smith RL, Fleischbein J (2002) The coastal ocean off Oregon and northern California during the 1997–8 El Niño. Prog Oceanogr 54:311–341

Kalnay R, Kanamitsu M, Kistler R, Collins W, Deaven D, Gandin L, Iredell M, Saha S, White G, Woollen J, Zhu Y, Leetmaa A, Reynolds R, Chelliah M, Ebisuzaki W, Higgins W, Janowiak J, Mo KC, Ropelewski C, Wang J, Jenne R, Joseph D (1996) The NCEP/NCAR 40-year reanalysis project. Bull Am Meteorol Soc 77:437–471

Kim SY, Kosro PM (2013) Observations of near-inertial surface currents off Oregon: decorrelation time and length scales. J Geophys Res 118(7):3723–3736. doi:10.1002/jgrc.20235

Kim SY, Kosro PM, Kurapov AL (2014) Evaluation of directly wind-coherent near-inertial surface currents off Oregon using a statistical parameterization and analytical and numerical models, J. Geophys. Res. in press

Kosro PM (2005) On the spatial structure of coastal circulation off Newport, Oregon, during spring and summer 2001, in a region of varying shelf width. J Geophys Res 110:C10S06. doi:10.1029/2004JC002769

Kosro PM, Barth JA, Strub PT (1997) The coastal jet: observations of surface currents along the Oregon continental shelf from HF radar. Oceanography 10(2):53–56

Kurapov AL, Egbert GD, Allen JS, Miller RN, Erofeeva SY, Kosro PM (2003) M2 internal tide off Oregon: inferences from data assimilation. J Phys Oceanogr 33:1733–1757

Kurapov AL, Foley D, Strub PT, Egbert GD, Allen JS (2011) Variational assimilation of satellite observations in coastal ocean model off Oregon. J Geophys Res 116, C05006. doi:10.1029/2010JC006909

Lee T, Fukumori I, Tang B (2004) Temperature advection: internal versus external processes. J Phys Oceanogr 34:1936–1944

MacCready P, Banas NS, Hickey BM, Dever EP, Liu Y (2009) A model study of tide- and wind-induced mixing in the Columbia river estuary and plume. Cont Shelf Res 29:278–291

Mantua NJ, Hare SR, Zhang Y, Wallace JM, Francis RC (1997) A Pacific interdecadal climate oscillation with impacts on salmon production. Bull Am Meteorol Soc 78:1069–1079

Marchesiello P, McWilliams JC, Shchepetkin A (2001) Ocean boundary conditions for long-term integration of regional ocean models. Ocean Mod 3:1–20

Mazzini PLF, Barth JA, Shearman RK, Erofeev A 2014 Buoyancy-driven coastal currents off the Oregon coast during fall and winter. J. Phys. Oceanogr. In press

McPhaden MJ (1999) Genesis and evolution of the 1997–98 El Niño. Science 283:950–954

Mellor GL, Yamada T (1982) Development of a turbulence closure model for geophysical fluid problems. Rev Geophys Space Phys 20:851–875

Osborne J, Kurapov AL, Egbert G, Kosro PM (2011) Spatial and temporal variability of the M2 internal tide generation and propagation on the Oregon shelf. J Phys Oceanogr 41:2037–2062

Osborne JJ, Kurapov AL, Egbert GD, Kosro PM (2014) Intensified diurnal tides along the Oregon coast. J Phys Oceanogr 44:1689–1703

Ramp SR, Bahr FR (2008) Seasonal evolution of the upwelling process south of Cape Blanco. J Phys Oceanogr 38:3–28

Schwing FB, Murphree T, deWitt L, Green PM (2002) The evolution of oceanic and atmospheric anomalies in the northeast Pacific during the El Niño and La Niña events of 1995–2001. Progr Oceanogr 54:459–491

Shchepetkin AF, McWilliams JC (2003) A method for computing horizontal pressure-gradient force in an oceanic model with a non-aligned vertical coordinate. J Geophys Res 108(C3):3090

Shchepetkin AF, McWilliams JC (2005) The regional oceanic modeling system (ROMS): a split-explicit, freesurface, topography-following-coordinate oceanic model. Ocean Model 9:347–404

Sutherland DA, MacCready P, Banas NS, Smedstad LF (2011) A modeling study of the Salish Sea estuarine circulation. J Phys Oceanogr 1125–1143

Todd RE, Rudnick DL, Davis RE, Ohman MD (2011) Underwater gliders reveal rapid arrival of El Niño effects off California's coast. Geophys Res Lett 38:L03609

Walters HM (2014) Relationship between winter downwelling and conditions and summer hypoxia severity along the Oregon coast. BSc Thesis, Oregon State Univ, p 40

Whitney MM, Allen JS (2009a) Coastal wind-driven circulation in the vicinity of a bank. Part I: modeling flow over idealized symmetric banks. J Phys Oceanogr 39:1273–1297

Whitney MM, Allen JS (2009b) Coastal wind-driven circulation in the vicinity of a bank. Part II: modeling flow over the Heceta Bank complex on the Oregon coast. J Phys Oceanogr 39:1298–1316

Wolter K (1987) The Southern Oscillation in surface circulation and climate over the tropical Atlantic, Eastern Pacific, and Indian Oceans as captured by cluster analysis. J Clim Appl Meteorol 26:540–558